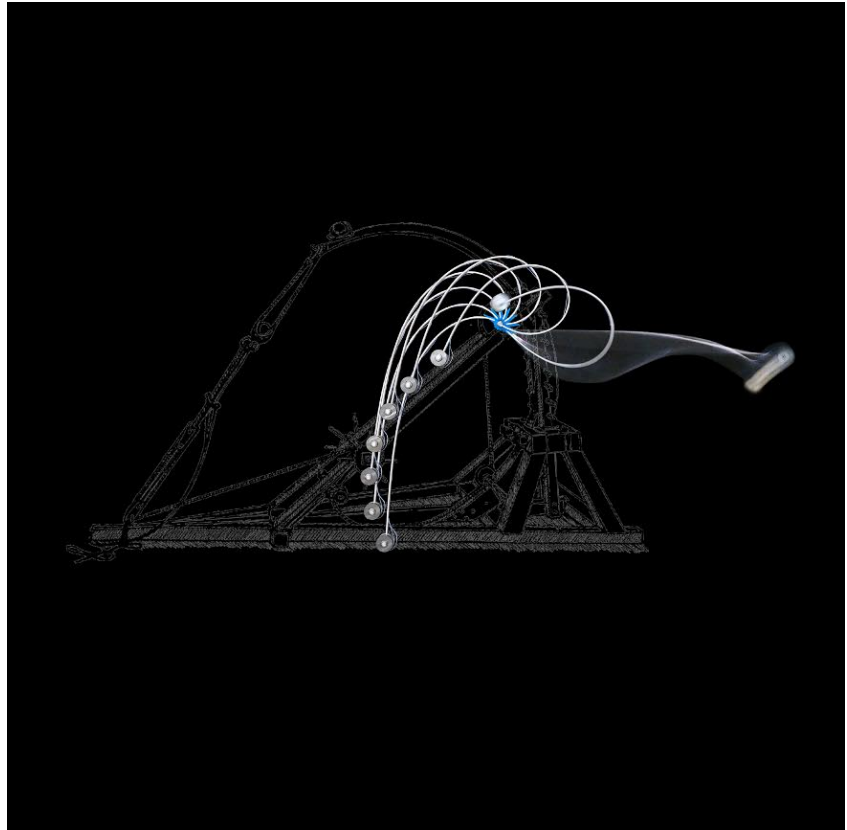




Costanza Armanini

Instabilities and dynamics of elastic rods in the presence of movable constraints



A new trend in the mechanical design of devices for advanced technologies, such as soft robotics and micro/nano mechanics, is the exploitation of structures undergoing large deflections, in an attempt of achieving superior performances. Within this framework, non-linear modelling becomes a fundamental tool for the design of compliant structures and deformable mechanism. Two structural systems are investigated, both based on the planar elastica and subject to movable and configurational constraints. These two structures disclose unforeseen behaviours when the values of the parameters defining the models are varied. The first structural system is an elastic rod constrained by a slowly rotating clamp, while the other end is loaded with a lumped mass weight. When this weight is lower than that corresponding to buckling, the edge of the rod describes a closed curve, behaving as an *elastica compass*. Differently, when the load is higher than that of buckling, a release of elastic energy is observed, leading to a snap-back of the structure, so that the rod realizes an *elastica catapult*. The clamp in the above described structure is replaced by a frictionless and fixed sliding sleeve in the second system considered in this thesis. The rod is subject to a sudden release from the underformed configuration, providing dynamic effects on the system. By means of the variational approach, the presence of a configurational force at the exit of the sliding sleeve is proven within the dynamical setting, extending previous results restricted to the quasi-static assumption. The configurational force is found to strongly affect the dynamics of the structure. In particular, two different behaviours are observed, in which the rod may either completely penetrate in ("injection") or be expelled from ("ejection") the sliding sleeve. In both the above problems, the theoretical predictions are corroborated through the experimental validation on physical models, which have been ad hoc invented and designed. A new insight is obtained in the design of flexible devices, paving the way to applications in soft robotics.

UNIVERSITY OF TRENTO - Italy
Department of Civil, Environmental
and Mechanical Engineering



Doctoral School in Civil, Environmental and Mechanical Engineering
Topic 3. Modelling and Simulation - XXX cycle 2014/2017

Doctoral Thesis - April 2018

Costanza Armanini

Instabilities and dynamics of elastic rods in the presence of movable constraints

Supervisors

Prof. Davide Bigoni, University of Trento

Dott. Francesco Dal Corso, University of Trento

Co-supervisor

Dott. Diego Misseroni, University of Trento



Except where otherwise noted, contents on this book are licensed under a Creative
Common Attribution - Non Commercial - No Derivatives
4.0 International License

University of Trento
Doctoral School in Civil, Environmental and Mechanical Engineering
<http://web.unitn.it/en/dricam>
Via Mesiano 77, I-38123 Trento
Tel. +39 0461 282670 / 2611 - *dicamphd@unitn.it*

Acknowledgements

First and foremost, I am deeply grateful to Prof. Davide Bigoni for giving me the opportunity to fulfil this Ph.D. research under his supervision. I thank him for the many advices and inspirations he has provided me throughout my time as his student.

I would like to thank Dott. Francesco Dal Corso, for his invaluable time, his patient guidance and for keeping me motivated throughout the ups and (expecially) the downs of this research. My sincere thanks goes also to Dr. Diego Misseroni, for his work in the experimental analysis that played an essential role in the development of my research but also for his continued support.

I would like to express my sincere gratitude to all the members of the Solid and Structural Mechanics Group, the colleagues and friends that I have met and with whom I've spent my daily life during my Ph.D. I would like to thank especially Gianluca and Alice whose friendship has been fundamental throughout these years. Finally, I thank Leonardo for his love and for always being extremely supportive and understanding. I want to express my very gratitude to my family and expecially to my parents for their never ending support and encouragement.

Support from the ERC Advanced Grant "Instabilities and non-local multiscale modelling of materials" 340561-FP7-PEOPLE-IDEAS-ERC-2013-AdG (2014-2019) is gratefully acknowledged.

Contents

Declaration of Authorship	iii
Acknowledgements	v
Introduction	9
I From the elastica compass to the elastica catapult	9
1 Introduction	11
2 Formulation	15
2.1 Total potential energy and the elastica equation . . .	17
3 Quasi-static response	21
3.1 Large displacement solution	22
3.2 Displacement field	24
3.3 Stability of the solutions	26
4 The elastica compass and the elastica catapult	31
4.0.1 Self intersection limit	34
4.1 The elastica compass	36
5 Robot's arm performance and design	43
5.1 Energy release	50

6 Snap-back dynamics	53
6.1 Massless rod model	54
Initial conditions	57
6.2 Finite element analysis	59
7 Experiments vs modelling	61
8 Conclusions and main scientific output	67
II Configurational forces within a dynamic framework	69
9 Introduction	71
10 Formulation	73
10.1 Kinematics	74
10.2 Lagrangian and governing equations from variational approach	77
10.3 Presence of the configurational force in dynamics	81
11 The evolution of an undeformed rod suddenly released	83
11.1 The closed-form spatial integration	84
12 The numerical integration in time	89
12.1 Initial conditions and small displacement regime .	91
12.1.1 Dimensionless parameters and numerical integration	94
13 Theoretical predictions and definition of p_{cr}	97
14 Experimental analysis	105
15 Conclusion	111

List of Figures

1	Drawings of catapults by Leonardo Da Vinci from <i>Codex Atlanticus</i> [11].	1
2	The mechanical system considered in Part I . An elastic rod has attached a lumped mass m at one end and is constrained at the other end by a slowly rotating clamp, inclined at an angle $\alpha(t)$ (increasing function of time t) with respect to the direction of the gravity.	3
3	Superposition of a stroboscopic photo of the considered structure during an experiment (realised in the Instabilities Lab of the University of Trento) and one of the da Vinci's catapults.	4
4	Trajectories travelled by the loaded ends of three soft robot arms with same bending stiffness B , subject to the same weight P but with differ in the soft arm length. It is noted that the maximum distance is not attained by the system having the maximum length.	5
5	The mechanical system considered in Part II . A rod is constrained by a frictionless sliding sleeve inclined by an angle α with a lumped mass m attached at the other end. The part of the rod outside the sliding sleeve, $\ell(t)$, represents the configurational parameter that rules the behaviour of the system.	6
6	The experimental set-up realised to investigate the dynamical behaviour of the system described in Part II	7

- 2.1 An elastic rod of length l , with bending stiffness B and linear mass density γ , has attached a lumped mass m at one end and is constrained at the other end by a slowly rotating clamp, inclined at an angle $\alpha(t)$ (increasing function of time t) with respect to the direction of the gravity. The rotation of the rod's axis with respect to the undeformed (straight) configuration is measured through the angle $\theta(s, t)$, with s being the curvilinear coordinate, $s \in [0, l]$. The $\hat{x} - \hat{y}$ and $x - y$ reference systems are reported, both centered at the clamp point, the former attached to the rotating clamp while the latter fixed as the loading direction. The polar coordinates $r - \varphi$ defining the rod's end position are also reported. . . . 15
- 4.1 Rotation of the loaded end of the rod $\theta_l + \alpha$ versus clamp angle α for different ratios P/P_{cr} , $\{0.5, 1, 3\}$ (left part) and $\{5, 8, 9.161\}$ (right part), showing the possibility of multiple equilibrium configurations (whenever $P > P_{cr}$) for sets of value of the clamp inclination α . Stable configurations are reported as continuous lines. Unstable equilibrium configurations associated to the first ($n = 1$) and second ($n = 2$) mode are reported as dashed and dotted lines, respectively. Deformed equilibrium configurations for the loading condition $P = 3P_{cr}$ are reported enclosed in green circles at different clamp rotations, when only one equilibrium configuration is possible ($\alpha_1 = \pi/4$ and $\alpha_3 = 7\pi/4$) and when two equilibrium configurations are possible ($\alpha_{2A} = \alpha_{2B} = \alpha_s = 1.348\pi$). . . . 32
- 4.2 Clamp inclination α_s , for which snap-back is attained, as a function of the load ratio P/P_{cr} . The theoretical prediction (continuous green line) is compared to the numerical evaluation (squares and triangles) obtained from the dynamic analysis (see Chapter 6) and the experimental data (circles) measured on the developed prototype (see Chapter 7). . . . 34

- 4.3 A sequence of quasi-static configurations of the elastica catapult ($P/P_{cr} > 1$) at increasing the clamp angle α for different values of P/P_{cr} ending with snap in the equilibrium configuration. The self-intersection of the rod occurring for $P \geq P_{si}$ is displayed. In particular, the limit case of self-intersection is shown in the central sequence ($P = P_{si} \approx 9.161P_{cr}$) while self-intersection is shown in the lower sequence ($P = 12P_{cr}$). 35
- 4.4 'Pencil lead' trajectories drawn by the elastica compass/catapult within the dimensionless plane $x/l-y/l$ for different values of P/P_{cr} . Stable configurations are reported as continuous lines. Unstable positions are marked as discontinuous lines, dashed lines for the first mode and dotted lines for the second mode. Deformed configurations of the elastic rod for specific end positions are reported in the circles on the left for the case $P = 3P_{cr}$ 36
- 4.5 'Pencil lead' position of the elastica compass/catapult described in terms of the radius r (upper part) and the angle φ (lower part) as functions of the clamp angle α for different load ratios P/P_{cr} , $\{0.1, 0.5, 1, 1.5, 3\}$ (left part) and $\{5, 8, 9.161\}$ (right part). Unstable configurations are reported as discontinuous lines, dashed and dotted for first and second mode configurations, respectively. 38

4.6 Maximum polar angle φ_{max} (red/dashed line) and polar angle at the verge of the snap-back instability φ_s (blue/continuous line) as functions of the load ratio P/P_{cr} (left). The two polar angles coincide for the range $P/P_{cr} \leq 8.3$. Initial part of the trajectory (dashed lines) travelled by the loaded end of three soft robot arms reported within the dimensionless plane $x\sqrt{P/B}-y\sqrt{P/B}$. The three systems have the same bending stiffness B , are subject to the same weight P , but differ in the soft arm length, $l = \{3.405, 4.005, 4.605\}\sqrt{B/P}$ (right). The deformed configurations of the three systems are drawn (continuous line) for clamp inclinations $\alpha = \{0.826, 0.997, 1.239\}\pi$, respectively, for which the hanged load lies along the polar coordinate $\varphi = \pi/4$. The maximum radial distance r_{max} is attained with the system having the length $l = 4.005\sqrt{B/P}$ 39

4.7 Reaction moment $M(0)$ at the clamp at varying clamp angle α for different values of the load ratio P/P_{cr} equal to $\{0.1, 0.5, 1, 1.5, 3\}$ (upper part) and to $\{5, 8, 9.161\}$ (lower part). Moments evaluated at unstable configurations are reported as discontinuous lines, dashed and dotted for first and second mode configurations, respectively. 41

5.1 Maximum horizontal distance d_x , maximum height d_y , and minimum radial distance r_{min} (upper part) and corresponding angles α_x, α_y , and α_r (lower part) plotted as functions of the load ratio P/P_{cr} . The distance d_h , equation (5.2), called ‘longest horizontal reach’ [39], the related angle α_h , and the snap angle curve α_s are also reported. 44

5.2	<i>Optimal load ratio P/P_{cr} as a function of the polar coordinate φ for which equation (5.3) is maximized (upper part, left). Maximum radial distance r_{max} normalized through division by the length l (upper part, right) and corresponding clamp inclination α (lower part, left) as functions of the angle φ. Arm length l and the maximum radial distance r_{max} (made dimensionless through division by the fixed parameters P and B) at varying the polar angle φ (lower part, right).</i>	48
5.3	<i>Energy difference $\Delta\mathcal{E}$, equation (5.12), normalized through division by B/l, as a function of the load ratio P/P_{cr} and the clamp inclination α (left part). Energy release \mathcal{E}_R at snap-back ($\alpha = \alpha_s$), equation (5.16), as a function of the load ratio P/P_{cr} (right part).</i>	51
6.1	<i>Free-body diagram of the massless rod model: schemes of the massless elastic rod (left) and the lumped mass (right). Regularization of the solution obtained with this simplified model is achieved through the introduction of the viscous coefficient c due to air drag and the finite stiffness k_c of the clamp.</i>	54
7.1	<i>Experimental setup for the elastica compass and the elastica catapult. (a) Global view of the experimental setup, (b) detail of the elastic rod, and (c) rear view detail of the rack and pinion mechanism to impose clamp rotation and from which the rotary position sensor is visible.</i>	62
7.2	<i>Comparison between the theoretically predicted and experimentally measured values of the moment at the clamp $M(0)$ at varying the clamp angle α for the elastica compass, in the case $P = 0.805P_{cr}$.</i>	63

7.3 Comparison between the theoretically predicted and experimentally measured values of the moment at the clamp $M(0)$ (upper part) and of the total acceleration of the lumped mass $a(l, t) = \sqrt{\ddot{x}(l, t)^2 + \ddot{y}(l, t)^2}$ (lower part) at varying the clamp angle α for the elastica catapult in the cases $P = 1.142P_{cr}$ (left column) and $P = 7.795P_{cr}$ (right column). The curves highlight the presence of snap-back dynamics during the clamp rotation when the angle α_s is approached. In particular, a change in sign for the moment at the clamp $M(0)$ is observed as well as high acceleration of the rod's end after the snap-back phenomena. 64

7.4 Superimposed photos at different clamp angles α for (a) the elastica compass, $P/P_{cr} = 0.805$, and (b) the elastica catapult, $P/P_{cr} = 7.795$. The blurred images in the photo on the right were taken during the post-snap dynamics at $1/20$ s shutter speed. The theoretical trajectory of the 'pencil lead', obtained from the quasi-static analysis, is reported as continuous yellow line. 66

10.1 An inextensible rod of total length l , bending stiffness B and linear mass density γ is constrained by a frictionless sliding sleeve inclined by an angle α . A lumped mass m is attached at the other end of the rod, providing a weight $P = mg$. The part of the rod outside the sliding sleeve is measured through $\ell(t)$, with $\ell_0 = \ell(t = 0)$ representing the length at the initial time $t = 0$. The rotation of the rod's axis with respect to the undeformed straight configuration is measured through the rotation field $\theta(s, t)$, with s being the curvilinear coordinate, $s \in [0, l]$. The reference systems $\hat{x} - \hat{y}$ and $x - y$ are reported, both centered at the exit of the sliding sleeve. The configurational force $M^2/2B$ is realized at the exit of the sliding sleeve. 73

- 13.1 Trajectories of the suddenly released mass within the dimensionless plane $x/\ell_0 - y/\ell_0$ for $\alpha = 15^\circ$ (first line), $\alpha = 30^\circ$ (second line) different values of the dimensionless load $p = \{0.5, 0.999, 1.001, 1.5\} p_{cr}(\alpha)$ where the load values are increased from the left to the right. The critical dimensionless loads are numerically computed to be approximately $p_{tr}(\alpha = 15^\circ) \simeq 9.87$, $p_{tr}(\alpha = 30^\circ) \simeq 3.74$. Deformed configurations are reported, attained at the dimensionless times $\tau_1 = 0.2$, $\tau_2 = 2$ and $\tau_3 = 3$ 100
- 13.2 Trajectories of the suddenly released mass within the dimensionless plane $x/\ell_0 - y/\ell_0$ for $\alpha = 45^\circ$ (first line) and $\alpha = 60^\circ$ (second line) at different values of the dimensionless load $p = \{0.5, 0.999, 1.001, 1.5\} p_{tr}(\alpha)$ where the load values are increased from the left to the right. The critical dimensionless loads are numerically computed to be approximately $p_{tr}(\alpha = 45^\circ) \simeq 1.84$ and $p_{tr}(\alpha = 60^\circ) \simeq 0.946$. Deformed configurations are reported, attained at the dimensionless times $\tau_1 = 0.2$, $\tau_2 = 2$ and $\tau_3 = 3$ 101
- 13.3 Map of the regions identifying the pairs of dimensionless load p and sliding sleeve inclination α for which injection ($p < p_{tr}$, green region) and ejection ($p \geq p_{tr}$, yellow region) occur when an undeformed rod at rest is suddenly released. The transition between these two behaviours is defined by the curve $p_{tr}(\alpha)$. Experimental results are also reported (see Chapter 14). 102
- 13.4 (Left part) Evolution in the dimensionless time τ is reported for of the external length $\ell(\tau)$ at different values of the sliding sleeve inclination, $\alpha = \{15^\circ, 30^\circ, 45^\circ, 60^\circ\}$ and values of the dimensionless load $p = \{0.1, 0.5, 0.999, 1, 1.001, 1.5\} p_{tr}(\alpha)$. (Right part) For the same values of α , phase portrait of $\ell(\tau)$, namely how the velocity $\dot{\ell}(\tau)$ varies with $\ell(\tau)$, is reported for $p = \{0.1, 0.999, 1, 1.001, 1.5\} p_{tr}(\alpha)$ 104

14.1	The experimental set-up realised to investigate the dynamical behaviour of the considered structural system. Insets (a) and (b) report the details of the release mechanism and the sliding sleeve realization, respectively.	105
14.2	Results of the test obtained for $p = 0.75p_{cr}$ (upper part) and $p = 1.1p_{cr}$ (lower part) for $\alpha = 45^\circ$. The experimental test confirm the transition between the two possible behaviours theoretically predicted.	107
14.3	Comparison between the trajectory travelled by the lumped mass during an experimental test performed with the carbon rod and that predicted by the theoretical analysis, obtained for $\alpha = 60^\circ$ and for a dimensionless load $p = 0.75p_{cr}$	108

Introduction

The Euler formula for the buckling of an elastic rod first appeared in 1774 in his paper *De Curvis Elasticis*, presented as an Appendix to the treatise on the calculus of variations *Treatise on Isoperimeters*. Such a formula probably represents the greatest example of how mathematics can be applied to mechanical problems, so that, not only the value of the critical load for a compressed rod was given, but also the equation describing the configuration of an elastic rod subject to terminal loads. The problem of flexural deformation of a rod caught the attention of many of the brightest minds in the history of mechanics, including Galileo and Bernoulli, so that its study might nowadays appear out of date.

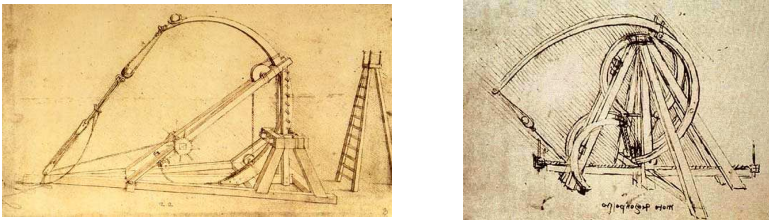


FIG. 1: Drawings of catapults by Leonardo Da Vinci from *Codex Atlanticus* [11].

Nevertheless, a great number of recent scientific results show that the study of the *elastica* is still worth. In particular, the

design of innovative devices for advanced applications is being driven by the need for compliant mechanisms, which are usually inspired by nature [22, 23] and are part of a transition from traditional robotics to soft-robotics, where the capability of (large) deflections of structural systems is exploited in order to maximize their performances [27, 32, 35]. In this scenario, the development of non-linear mechanical models, as those described by the Euler's *Elastica*, becomes a fundamental tool in the design of compliant devices and represents the main focus of the present Ph.D. thesis, with the purpose of disclosing and describe unforeseen mechanical response that can be exploited in the design of innovative devices.

In the first part of the thesis ¹, the development of basic mechanical model is addressed for the prediction of the behaviour of highly flexible robot arms. The possibility of exploiting the elastic deflection of rods was first considered by Leonardo da Vinci [11], who in his *Codex Atlanticus* drew a series of "elastic catapults", which yield a significant increase in the throwing distance, through a release of inflexional elastic energy.

Inspired by da Vinci's drawings, the mechanics of an elastic rod clamped at one end and subject to a dead load at the other is investigated (Chapter 2). Starting from the straight vertical configuration, corresponding to a uniform tensile loading condition, the clamp is slowly rotated so that the system displays a sequence of deformed configurations in which the rod is bent.

When the dead load, provided by the weight of a lumped mass, is lower than that corresponding to buckling of the structure in its straight configuration, the systems does not suffer any instability and a continuous smooth sequence of deformed configurations is obtained, with the edge of the rod describing a closed curve, similar to (but different from!) a circle, so

¹C. Armanini, F. Dal Corso, D. Misseroni and D. Bigoni, "From the elastica compass to the elastica catapult: an essay on the mechanics of soft robot arm". In: *Proceedings of the Royal Society A*, (2017), **473**,20160870. Cover paper.

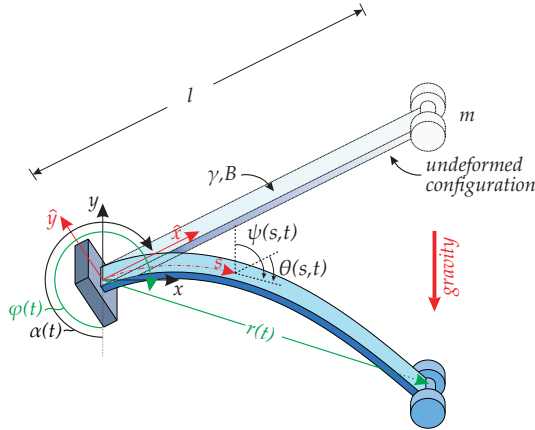


FIG. 2: The mechanical system considered in **Part I**. An elastic rod has attached a lumped mass m at one end and is constrained at the other end by a slowly rotating clamp, inclined at an angle $\alpha(t)$ (increasing function of time t) with respect to the direction of the gravity.

that the structure behaves as an "*elastica compass*". When the load is higher than that for buckling, the continued rotation of the clamp leads to an unstable configuration (characterized by a specific angle for the clamp inclination), so that the system spontaneously displays a sudden release of elastic energy and snaps to a non-adjacent configuration, in such a way that the structure behaves as an "*elastica catapult*", perhaps resembling the da Vinci's drawings (see Fig. 3).

The critical values of the angle of the clamped end, corresponding to the snap-back instability, are defined from the analysis of the quasi-static loading path described in a closed form by means of Elliptic functions (Chapter 3), through an extension of results pioneered by Wang [38]. Moreover, the dynamic behaviour during the snap is investigated through an ad hoc formulated numerical model, where the rod is reduced to a non-linear spring governed by the equation of the elastica. The

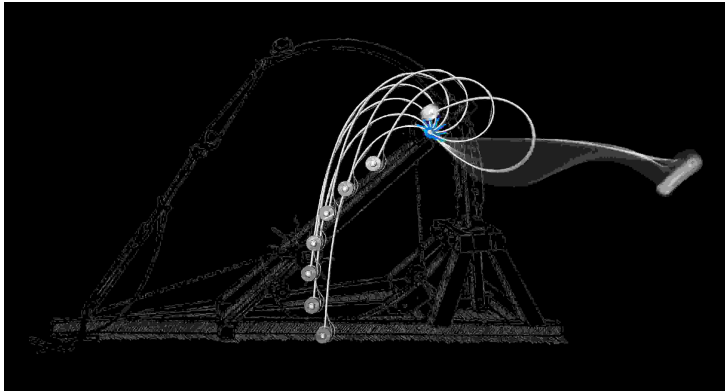


FIG. 3: Superposition of a stroboscopic photo of the considered structure during an experiment (realised in the Instabilities Lab of the University of Trento) and one of the da Vinci's catapults.

set-up of a numerical technique is a complex problem, which was analyzed from several points of view [16, 17, 19, 20, 28, 33], but not still completely solved. In particular, the proposed approach is developed as an extension of a previous work [34], which was conceived for pneumatic soft robot arms. The implemented procedure is also supported by results from a classical finite element analysis, obtained with the software Abaqus (Chapter 6). The presented solution represents a useful tool in the design of a soft robot arm, whose performances are investigated in terms of the distances that can be reached and the elastic energy that can be released from the catapult behaviour (Chapter 5).

The second part of the thesis is devoted to the analysis of the action of configurational forces on structural systems within a dynamic setting. Configurational forces, which were first introduced by Eshelby ([12] [13] [14] and [15]), arise when a structure is free of changing his configuration. It has been demonstrated

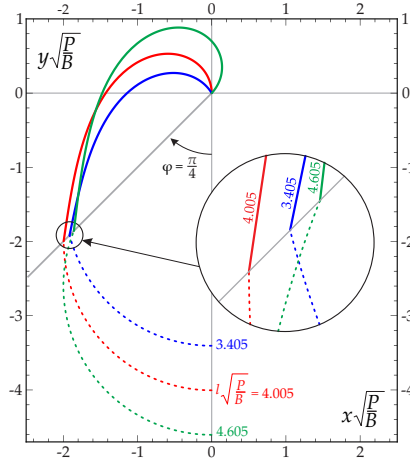
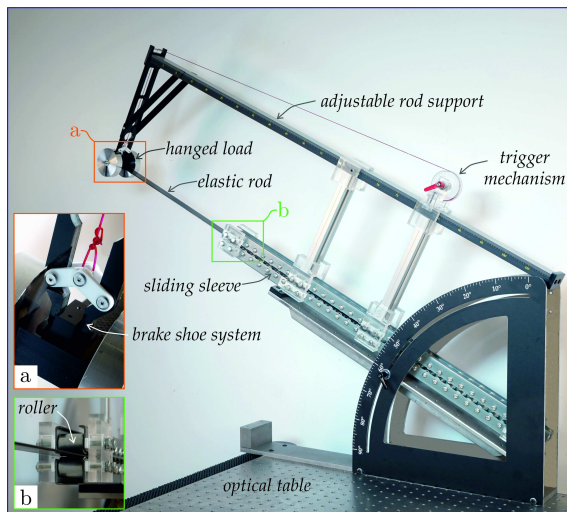


FIG. 4: Trajectories travelled by the loaded ends of three soft robot arms with same bending stiffness B , subject to the same weight P but with differ in the soft arm length. It is noted that the maximum distance is not attained by the system having the maximum length.

([6], [7]) that *in statics* they similar forces arise when a perfectly smooth sliding sleeve is applied to an end of an elastic rod.

In the second part of the thesis, the rotational clamp of the first problem analyzed is replaced by a sliding sleeve, while now the weight at the other end of the rod is assumed to be instantaneously released at a certain instant of time from a fully unloaded configuration. An extension of the numerical procedure used to describe the snap-back dynamics of the elastic catapult is employed to analyze the dynamics of the rod with the sliding sleeve. A spatial integration of the elastica is performed to investigate the behaviour of such a non-linear dynamical system, dependent on a configurational parameter, namely, the length of the part of the rod outside the constraint. The presence of a configurational force is demonstrated within the dynamical setting (using a variational approach) and it is



The experimental set-up realised to investigate the dynamical behaviour of the system described in **Part II**

described with a great accuracy. This concepts are ready to be exploited in the design of innovative devices for advanced applications, as for example in soft robotics.

Part I

From the elastica compass to the elastica catapult

1 Introduction

The design of innovative devices for advanced applications is being driven by the need for compliant mechanisms, which are usually inspired by nature [22, 23] and are part of a transition from traditional robotics to soft-robotics [27, 32, 35]. Compliant mechanisms require the development and use of non-linear mechanical models such as the Kirchhoff rod [10] and Euler's elastica, which allow the description of large deflections in elastic bars and the modelling of snake locomotion [9, 36], as well as object manipulation [37, 40, 41], useful in robotic assistance during surgery [7, 26] and for physical rehabilitation [29].

In this first part of the thesis, a basic mechanical model for a soft robot arm is addressed through new theoretical, numerical, and experimental developments. In particular, the deformable mechanical system sketched in Fig. 10.1 is considered, in which an elastic rod is clamped at one end and subject to a dead load at the other. The load is provided by the weight of a mass predominantly higher than that of the rod. The clamp rotates slowly so that, starting from a configuration in which the rod is subject to purely tensile axial load, the system quasi-statically evolves in a number of elastic forms at varying clamp angle. When the load is inferior to that corresponding to buckling of the straight and uniformly compressed configuration, a whole quasi-static 360°-rotation of the clamp is possible and the edge of the rod describes a (smooth, convex and simple) closed curve, which is theoretically solved using Euler's elastica. In the case of a rigid rod, this curve would be a circle, so that the mechanical

system behaves as an ‘elastica compass’, thus tracing the curve described by the elastica. However, when the load is higher than which would lead to buckling for the straight rod, an unstable configuration is quasi-statically reached, at which the rod suffers a snap-back instability and dynamically approaches another configuration, so that the system behaves as an ‘elastica catapult’. The description of the quasi-static path of the system and the determination of the unstable configuration is solved in an analytical form by means of elliptic functions through an extension of results pioneered by Wang [38], who employed a numerical integration procedure and provided asymptotic estimates valid in some particular cases (very stiff and very compliant rods, and nearly vertical equilibrium configurations).

In addition to the quasi-static solution, the dynamics of the snap instability is addressed numerically. The set-up of a numerical technique is a complex problem, which was analyzed from several points of view, but not still completely solved [16, 17, 19, 20, 28, 33]. To this purpose, two approaches are presented, one is a standard use of a finite element software (Abaqus), while the other is developed as a perfection of a technique introduced for pneumatic soft robot arms [34]. The latter approach, in which the elastic rod is reduced to a non-linear spring governed by the elastica, is elegant, but the kinematics is limited to the first deformation mode and an axial deformation and viscous damping have to be added to prevent spurious numerical instabilities, issues which may be circumvented through the finite element approach.

Finally, the experimental validation of the elastic system was performed using a mechanical setup specifically designed and realized at the ‘Instabilities Lab’ of the University of Trento. Experimental results fully validate the theoretical modelling, thus confirming that the elastica allows for solutions useful in the kinematics of a soft robot arm. The performance of the robot

arm is also assessed in terms of (i.) the maximum and minimum distances that can be reached without encountering loss of stability of the configuration, and (ii.) the maximum energy release that can be achieved when the system behaves as a catapult. These results open the way to a rational design of deformable robot arms and, as a side development, may find also application in the analysis of the pole vault dynamics and the optimization of athletes' performance [18], [21].

2 Formulation

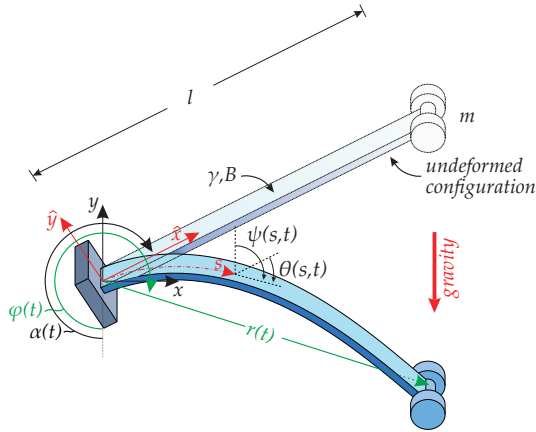


FIG. 2.1: An elastic rod of length l , with bending stiffness B and linear mass density γ , has attached a lumped mass m at one end and is constrained at the other end by a slowly rotating clamp, inclined at an angle $\alpha(t)$ (increasing function of time t) with respect to the direction of the gravity. The rotation of the rod's axis with respect to the undeformed (straight) configuration is measured through the angle $\theta(s, t)$, with s being the curvilinear coordinate, $s \in [0, l]$. The $\hat{x} - \hat{y}$ and $x - y$ reference systems are reported, both centered at the clamp point, the former attached to the rotating clamp while the latter fixed as the loading direction. The polar coordinates $r - \varphi$ defining the rod's end position are also reported.

An inextensible planar rod with bending stiffness B , total length l , linear mass density γ , and straight in its undeformed configuration, has a lumped mass m attached at one end while the other end is constrained by a clamp having inclination $\alpha(t)$ with respect to gravity direction, Fig. 2.1.

The clamp angle $\alpha(t)$ smoothly and slowly increases in time t , so that a quasi-statically rotating clamp is realized. The rotation of the rod's axis with respect to the undeformed (straight) configuration is denoted by $\theta(s, t)$, function of the time t and of the curvilinear coordinate $s \in [0, l]$, with $s = 0$ singling out the position of the clamp, where $\theta(0, t) = 0$, and $s = l$ of the loaded rod's end.

With respect to the undeformed straight configuration, 'frozen' at the inclination angle $\alpha(t)$, the coordinates $\hat{x}(s, t)$ and $\hat{y}(s, t)$ measure the position of the rod's axis in the rotating system, and, due to the inextensibility condition, are connected to the rotation field through the following differential relations [2]

$$\begin{aligned}\hat{x}'(s, t) &= \cos \theta(s, t), \\ \hat{y}'(s, t) &= -\sin \theta(s, t),\end{aligned}\tag{2.1}$$

where a prime denotes the derivative along the curvilinear coordinate s . The position can be described through the coordinates $x(s, t)$ and $y(s, t)$ (the former orthogonal and the latter parallel, but with opposite direction, to the gravity), which are connected with the positions $\hat{x}(s, t)$ and $\hat{y}(s, t)$ through the following relationships

$$\begin{aligned}x(s, t) &= -\hat{x}(s, t) \sin \alpha(t) + \hat{y}(s, t) \cos \alpha(t), \\ y(s, t) &= -\hat{x}(s, t) \cos \alpha(t) - \hat{y}(s, t) \sin \alpha(t),\end{aligned}\tag{2.2}$$

so that the kinematical constraint, equation (2.1), implies

2.1. Total potential energy and the elastica equation

$$\begin{aligned}x'(s, t) &= -\sin [\theta(s, t) + \alpha(t)], \\y'(s, t) &= -\cos [\theta(s, t) + \alpha(t)].\end{aligned}\tag{2.3}$$

During the rotation, the position of the clamp ($s = 0$) is considered fixed and taken as the origin of the reference systems

$$x(0, t) = y(0, t) = \hat{x}(0, t) = \hat{y}(0, t) = 0.\tag{2.4}$$

2.1 Total potential energy and the elastica equation

Denoting with g the gravitational acceleration, the rod is loaded by the weight P due to the lumped mass m , so that $P = mg$, and the rod distributed weight γg (the latter neglected in the quasi-static analysis). Neglecting the rotational inertia of the lumped mass and of the rod, the Lagrangian functional for the system is given by

$$\begin{aligned}\mathcal{L}(t) &= \mathcal{T}(t) - \mathcal{V}(t) + \\&- \int_0^l N_x(s, t) \{x'(s, t) + \sin [\theta(s, t) + \alpha(t)]\} ds + \\&- \int_0^l N_y(s, t) \{y'(s, t) + \cos [\theta(s, t) + \alpha(t)]\} ds,\end{aligned}\tag{2.5}$$

where

- $N_x(s, t)$ and $N_y(s, t)$, playing here the role of Lagrangian multipliers, represent the internal forces along the x and y directions;

- $\mathcal{T}(t)$ is the kinetic energy of the system, given by

$$\mathcal{T}(t) = \frac{1}{2}m[\dot{x}^2(l,t) + \dot{y}^2(l,t)] + \frac{1}{2} \int_0^l \gamma[\dot{x}^2(s,t) + \dot{y}^2(s,t)]ds, \quad (2.6)$$

where $[\dot{\cdot}]$ denotes the time derivative;

- $\mathcal{V}(t)$ is the sum of the elastic energy stored within the rod and the negative of the work done by the weight due to the lumped mass P and that by the rod distributed weight γg

$$\mathcal{V}(t) = \frac{1}{2} \int_0^l B\theta'(s,t)^2 ds + Py(l,t) + \int_0^l \gamma g y(s,t) ds. \quad (2.7)$$

The governing equations can be derived through the application of the least action principle on the functional

$$\mathcal{A}(t) = \int_{t_0}^{t^*} \mathcal{L}(t) dt, \quad (2.8)$$

with t_0 and t^* being arbitrary initial and final instants of the analysed time interval.

Reference is made to a perturbation in the fields $\{x(s,t), y(s,t), \theta(s,t)\}$ by means of the small parameter ϵ and of the field variations $\{x_{var}(s,t), y_{var}(s,t), \theta_{var}(s,t)\}$ satisfying the time and space conditions

$$\begin{aligned} x_{var}(s,t) = y_{var}(s,t) = \theta_{var}(s,t) = 0, & \quad \text{for } t = t_0 \text{ and } t = t^*, \\ x_{var}(0,t) = y_{var}(0,t) = \theta_{var}(0,t) = 0, & \quad t \in [t_0, t^*]. \end{aligned} \quad (2.9)$$

2.1. Total potential energy and the elastica equation

Therefore, the minimum of the functional $\mathcal{A}(t)$, equation (2.8), is obtained by imposing the following condition

$$\begin{aligned}
 & \int_0^l [\gamma \ddot{x}(s, t) - N'_x(s, t)] x_{var}(s, t) ds + \\
 & + \int_0^l \left\{ \gamma [g + \ddot{y}(s, t)] - N'_y(s, t) \right\} y_{var}(s, t) ds + \\
 & + \int_0^l \theta_{var}(s, t) \left\{ B\theta''(s, t) - N_x(s, t) \cos[\theta(s, t) + \alpha(t)] + \right. \\
 & \left. + N_y(s, t) \sin[\theta(s, t) + \alpha(t)] \right\} ds + \\
 & + [m\ddot{x}(l, t) + N_x(l, t)] x_{var}(l, t) + \\
 & + [m\ddot{y}(l, t) + P + N_y(l, t)] y_{var}(l, t) + \\
 & - B\theta'(l, t)\theta_{var}(l, t) = 0
 \end{aligned} \tag{2.10}$$

providing finally the differential system

$$\begin{cases}
 B\theta''(s, t) - N_x(s, t) \cos[\theta(s, t) + \alpha(t)] + N_y(s, t) \sin[\theta(s, t) + \alpha(t)] = 0, \\
 N'_x(s, t) = \gamma \ddot{x}(s, t), \\
 N'_y(s, t) = \gamma [g + \ddot{y}(s, t)],
 \end{cases} \tag{2.11}$$

and the boundary conditions

$$\begin{cases}
 \theta'(l, t) = 0, \\
 N_x(l, t) = -m\ddot{x}(l, t), \\
 N_y(l, t) = -m [g + \ddot{y}(l, t)].
 \end{cases} \tag{2.12}$$

Equation (2.11)₁ yield the differential equilibrium equation

for the elastica, demonstrating that N_x and N_y are the internal forces acting on the rod along the x and y directions.

3 Quasi-static response

When quasi-static conditions prevail, neglecting the weight of the rod γgl when compared to that of the lumped mass attached at the end of the rod P , the acceleration of the rod's axis can be omitted:

$$\ddot{x}(s, t) = \ddot{y}(s, t) = 0, \quad (3.1)$$

so that from the boundary conditions (2.12)₂ and (2.12)₃, and the differential equations (2.11)₂ and (2.11)₃, the rod's internal forces result to be constant along the rod

$$N_x(s, t) = 0, \quad N_y(s, t) = -P. \quad (3.2)$$

Omitting in this chapter the dependence on time t , finally the governing equation for the rotation field (2.11)₁, complemented with the boundary conditions, equation (2.12)₁, reduces to the *elastica* [2, 5]

$$\begin{cases} B\theta''(s) - P \sin[\theta(s) + \alpha] = 0, \\ \theta'(l) = 0, \\ \theta(0) = 0. \end{cases} \quad (3.3)$$

In order to solve the differential problem (3.3), the symbol $\lambda^2 = P/B$ and the auxiliary rotation $\psi(s) = \theta(s) + \alpha - \pi$, measuring the inclination of the rod tangent with respect to the y axis, (see Fig. 2.1), are introduced, so that the system (3.3) can be rewritten as:

$$\begin{cases} \psi''(s) + \lambda^2 \sin \psi(s) = 0, \\ \psi(0) = \alpha - \pi, \\ \psi'(l) = 0, \end{cases} \quad (3.4)$$

and therefore, integrating, the following differential equation is obtained

$$\frac{d\psi}{ds} = \pm \lambda \sqrt{2[\cos \psi(s) - \cos \psi(l)]}, \quad (3.5)$$

where only a positive curvature is considered, since it is found that the solution does not vary with the sign considered in equation (3.5).

It is a standard expedient to introduce the following substitutions:

$$\begin{aligned} k^2 &= \sin^2 \left(\frac{\psi(l)}{2} \right), \\ k^2 \sin^2 \sigma(s) &= \sin^2 \left(\frac{\psi(s)}{2} \right), \end{aligned} \quad (3.6)$$

in order to obtain, through trigonometric formulae, the final version of the differential problem:

$$\lambda \int_0^s ds = \int_{\sigma(0)}^{\sigma(s)} \frac{d\sigma}{\sqrt{1 - k^2 \sin^2 \sigma}}. \quad (3.7)$$

3.1 Large displacement solution

In order to obtain the expression providing the relationship between the applied load P and the deformation of the rod, represented by the rotation at the loaded end, $\theta(l) = \theta_l$, equation (3.7) must be integrated between $s = 0$ and $s = l$:

$$\lambda l = \int_{\sigma(0)}^{\sigma(l)} \frac{d\sigma}{\sqrt{1 - k^2 \sin^2 \sigma}} \quad (3.8)$$

3.1. Large displacement solution

where:

- when $s = 0$, $\psi(0) = \alpha - \pi$, so that from equation (3.6)₂

$$\sigma(0) = \arcsin \left[\frac{1}{k} \sin \left(\frac{\alpha - \pi}{2} \right) \right] + h\pi = \sigma_0 + h\pi, \quad (3.9)$$

with $h = 1, 2, 3, \dots$

- when $s = l$, $\psi(l) = \theta_l - \alpha - \pi$, so that from (3.6)₁

$$\sigma(l) = \frac{2j+1}{2}\pi, \quad (3.10)$$

with $j = 1, 2, 3, \dots$

and therefore, recalling that $\lambda^2 = P/B$, separating the variables and integrating equation (3.8) yields:

$$P = \frac{B}{l^2} [(2n-1)\mathcal{K}(k) - \mathcal{K}(\sigma_0, k)]^2. \quad (3.11)$$

In equation (3.11), $n = 1, 2, 3, \dots$ is an integer representing the n -th mode solution, while $\mathcal{K}(k)$ and $\mathcal{K}(\sigma_0, k)$ are, respectively, the complete and the incomplete elliptic integral of the first kind of modulus k :

$$\mathcal{K}(a, k) = \int_0^a \frac{d\sigma}{\sqrt{1 - k^2 \sin^2 \sigma}}, \quad \mathcal{K}(k) = \mathcal{K}\left(\frac{\pi}{2}, k\right). \quad (3.12)$$

In the following, the analysis is mainly addressed to the deformation mode $n = 1$, because only the equilibrium configurations related to this mode are stable [2], [24], as demonstrated in section (3.3). However, (when existing) the unstable equilibrium configurations related to deformation mode with $n \neq 1$

will also be considered in the case $P/P_{cr} > 4$ to provide the whole equilibrium paths of the system.

3.2 Displacement field

Considering equation (3.9), the integral on the right hand side of equation (3.7) can always be rewritten as

$$\int_{\sigma_0+h\pi}^{\sigma(s)} \frac{d\sigma}{\sqrt{1-k^2 \sin^2 \sigma}} = \int_0^{\sigma(s)} \frac{d\sigma}{\sqrt{1-k^2 \sin^2 \sigma}} - \mathcal{K}(\sigma_0, k) - 2h\mathcal{K}(k), \quad (3.13)$$

which finally provides

$$\sigma(s) = \text{Am}(s\lambda + \mathcal{K}(\sigma_0, k) + h\pi, k), \quad (3.14)$$

where $\text{Am}(\cdot, k)$ denotes the Jacobi amplitude function of modulus k . Considering the definition (3.6)₂, equation (3.14) yields to the following relation

$$\sin^2 \frac{\psi(s)}{2} = k^2 \text{Sn} [s\lambda + \mathcal{K}(\sigma_0, k), k], \quad (3.15)$$

where $\text{Sn}(\cdot, k)$ is the Jacobi sine amplitude function, defined as

$$\text{Sn}(a, k) = \sin[\text{Am}(a, k)]. \quad (3.16)$$

Employing the identities $\cos \psi = 1 - \sin^2 \psi/2$ and $\sin \psi = 2 \sin \psi/2 \sqrt{1 - \sin^2 \psi/2}$, the following relations are found

$$\cos \psi = 1 - 2k^2 \text{Sn}^2 [s\lambda + \mathcal{K}(\sigma_0, k), k], \quad (3.17)$$

$$\sin \psi = 2k \text{Sn} [s\lambda + \mathcal{K}(\sigma_0, k), k] \text{Dn} [s\lambda + \mathcal{K}(\sigma_0, k), k],$$

where $\text{Dn}(\cdot, k)$ is the Jacobi elliptic function, defined as

3.2. Displacement field

$$\text{Dn}(a, k) = \sqrt{1 - k^2 \text{Sn}^2(a, k)}. \quad (3.18)$$

Finally, recalling that $\psi(s) = \theta(s) + \alpha - \pi$, equations (3.17) can be introduced in equations (2.1) to obtain the differential problem determining the deformed elastica:

$$\begin{aligned} \hat{x}'(s) = +\cos\theta(s) &= -\cos\alpha[1 - 2k^2\text{Sn}^2[s\lambda + \mathcal{K}(\sigma_0, k), k]] + \\ &\quad -\sin\alpha\{2k\text{Sn}[s\lambda + \mathcal{K}(\sigma_0, k), k]\}, \\ \hat{y}'(s) = -\sin\theta(s) &= -\sin\alpha[1 - 2k^2\text{Sn}^2[s\lambda + \mathcal{K}(\sigma_0, k), k]] + \\ &\quad +\cos\alpha\{2k\text{Sn}[s\lambda + \mathcal{K}(\sigma_0, k), k]\}. \end{aligned} \quad (3.19)$$

Considering the following integration rules

$$\begin{aligned} \frac{\partial}{\partial\sigma}E(a, x) &= \sqrt{1 - k^2 \sin^2\sigma}, \\ \frac{\partial}{\partial\sigma}\text{Am}(a, x) &= \text{Dn}(a, k), \\ \frac{\partial}{\partial\sigma}\text{Cn}(a, x) &= -\text{Sn}(a, k)\text{Dn}(a, k), \end{aligned} \quad (3.20)$$

where $E(\cdot, x)$ is the incomplete elliptic integral of the second kind of modulus k

$$E(a, x) = \int_0^a \sqrt{1 - k^2 \sin^2\sigma} d\sigma, \quad (3.21)$$

and $\text{Cn}(\cdot, k)$ is the Jacobi cosine amplitude function, defined as

$$\text{Cn}(a, k) = \cos[\text{Am}(a, k)], \quad (3.22)$$

integration of the differential system (3.19) provides the position of the rod's axis in the $\hat{x} - \hat{y}$ reference system ([1], [25])

$$\begin{aligned}\hat{x}(s) &= -\cos \alpha A_1(s)l + \sin \alpha A_2(s)l, \\ \hat{y}(s) &= -\sin \alpha A_1(s)l - \cos \alpha A_2(s)l,\end{aligned}\tag{3.23}$$

where

$$\begin{aligned}A_1(s) &= -\frac{s}{l} + \frac{2}{\lambda l} \left\{ E(\text{Am}(s\lambda + \mathcal{K}(\sigma_0, k), k), k) - E(\sigma_0, k) \right\}, \\ A_2(s) &= +\frac{2k}{\lambda l} \left\{ \text{Cn}(s\lambda + \mathcal{K}(\sigma_0, k), k) - \text{Cn}(\mathcal{K}(\sigma_0, k), k) \right\}.\end{aligned}\tag{3.24}$$

On the other hand, since in the quasi-static solution the only applied load is the weight of the lumped mass P , having an inclination $\beta \equiv \alpha$, the position of the rod's axis in the fixed $x - y$ reference system becomes

$$\begin{aligned}x(s) &= -A_2(s)l, \\ y(s) &= +A_1(s)l.\end{aligned}\tag{3.25}$$

3.3 Stability of the solutions

The stability of the solutions can be evaluated by analysing the second variation of the total potential energy, equation (2.7), which, in the quasi-static analysis, can be written as follows

$$\frac{\mathcal{V}}{B} = \frac{1}{2} \int_0^l \theta'(s)^2 ds + \lambda^2 y(l) ds,\tag{3.26}$$

3.3. Stability of the solutions

where, from equation (2.3)₂, the vertical displacement at the free end of the beam can be evaluated as

$$y(l) = - \int_0^l \cos [\theta(s) + \alpha] ds. \quad (3.27)$$

Introducing a variation $\delta\theta(s)$ satisfying the boundary conditions

$$\delta\theta(0) = \delta\theta'(l) = 0, \quad (3.28)$$

and through integration by parts, the second variation of $\frac{\mathcal{V}}{B}$ can be evaluated as

$$\frac{\delta^2\mathcal{V}}{B} = - \int_0^l \{ \delta\theta''(s)\delta(s)\theta(s) - \lambda^2 \cos [\theta(s) + \alpha] \delta\theta^2(s) \} ds \quad (3.29)$$

for all admissible $\delta\theta(s)$. Finally, the stability criterion can be applied

$$\delta^2\mathcal{V} \begin{cases} > 0 & \text{stability} \\ < 0 & \text{instability} \end{cases} \quad (3.30)$$

In order to treat conditions (3.29) and (3.30), the non-trivial solutions of the Sturm-Liouville problem [8]

$$\begin{cases} \phi_n''(s) - \gamma_n \lambda^2 \cos [\theta(s) + \alpha] \phi_n(s) = 0, \\ \phi_n(0) = 0, \\ \phi_n'(l) = 0, \end{cases} \quad (3.31)$$

are considered, where $\phi_n(s)$ are the eigenfunctions associated to the eigenvalues γ_n with weight function

$$\lambda^2 \cos [\theta(s) + \alpha]. \quad (3.32)$$

It is known [2] that

- system (3.31) admits an infinite set of eigenvalues γ_n that can be arranged in an increasing sequence $\gamma_{n+1} > \gamma_n \forall$ integer n ;
- when $n \rightarrow \infty, \gamma_n \rightarrow \infty$;
- the eigenfunctions $\phi_n(s)$ are orthogonal with weight function $\cos [\theta(s) + \alpha]$

$$\int_0^l \phi_n(s) \phi_m(s) \cos [\theta(s) + \alpha] ds = 0 \quad n \neq m \quad (3.33)$$

These remarks define a norm and a weight orthogonality condition, so that the system $\phi_n(s)$ with weight function (3.32) can be used to give a (converging) Fourier series representation to the function $\delta\theta(s)$ with Fourier coefficients C_n

$$\delta\theta(s) \simeq \sum_{n=1}^{\infty} C_n \phi_n(s). \quad (3.34)$$

The Fourier representation can be substituted in equation (3.29) considering (3.31) to obtain

$$\frac{\delta^2 \mathcal{V}}{B} = \int_0^l \left[\sum_{n=1}^{\infty} (\gamma_n - 1) C_n \phi_n(s) \lambda^2 \cos [\theta(s) + \alpha] \right] \left[\sum_{m=1}^{\infty} C_m \phi_m(s) \right] ds, \quad (3.35)$$

so that the stability criterion (3.30) implies

$$\frac{\delta^2 \mathcal{V}}{B} = \sum_{n=1}^{\infty} C_n^2 \left(1 - \frac{1}{\gamma_n} \right) \int_0^l (\phi_n'(s))^2 ds \begin{cases} > 0 \rightarrow \gamma_n > 1 \cup \gamma_n < 0 \\ < 0 \rightarrow \gamma_n > 0 \cup \gamma_n < 1 \end{cases} \quad (3.36)$$

and therefore

$$\begin{cases} \gamma_n \notin [0, 1] & \longrightarrow \text{stability} \\ \gamma_n \in (0, 1) & \longrightarrow \text{instability} \end{cases} \quad (3.37)$$

3.3. Stability of the solutions

while the values $\gamma_n = 0$ and $\gamma_n = 1$ represent critical points.

In order to judge the stability of the deformed system, the weight function $\cos[\theta(s) + \alpha]$ can be evaluated from equation (3.15) as follows

$$\cos[\theta(s) + \alpha] = - \{ 1 - k^2 \operatorname{Sn}[(2n+1)\tilde{s}\lambda l + \mathcal{K}(\sigma_0, k), k] \}, \quad (3.38)$$

where the non-dimensional variable $\tilde{s} = s/l \in [0, 1]$ has been introduced, while λ can be evaluated from 3.11

$$\lambda = \frac{1}{l} [(2n-1)\mathcal{K}(k) - \mathcal{K}(\sigma_0, k)]. \quad (3.39)$$

Introducing (3.39) and (3.38) in (3.31)₁, the final expression of the Sturm Liouville problem is obtained

$$\begin{aligned} & \phi_n''(\tilde{s}) + \phi_n(\tilde{s})\gamma_n [(2n-1)\mathcal{K}(k) - \mathcal{K}(\sigma_0, k)]^2 + \\ & + \{ 1 - k^2 \operatorname{Sn}[(2n+1)\tilde{s}[(2n-1)\mathcal{K}(k) - \mathcal{K}(\sigma_0, k)] + \mathcal{K}(\sigma_0, k), k] \} \\ & = 0, \end{aligned} \quad (3.40)$$

so that for a given mode n and an inclination at rod's end θ_l , the smallest eigenvalue γ_n has to be determined as solution of 3.40 with the boundary condition 3.31₂ and 3.31₃. Such a problem can be solved with the numerical routine, based on the bisection method, that was proposed by [24]. The boundary conditions

$$\phi_n(0) = 0, \quad \phi_n'(0) = 1, \quad (3.41)$$

are considered in order to automatically remove the trivial solution of the problem and interactions on γ_n can be performed until the condition $\phi_n'(1) = 0$ is attained. Through this numerical procedure, it is found that:

- the first mode, $n = 1$, is always stable when P is lower than the buckling load P_{cr} of the purely compressed clamped

rod ($\alpha = \pi$);

- when $n = 1$ and $P \geq P_{cr}$, the elastica configurations are stable only when α falls within a specific range of values (as it is demonstrated in chapter 4);
- equilibrium configurations related to deformation modes with $n \neq 1$ seem to be unstable, as suggested by ([2]) and ([25]); however, with the proposed numerical procedure, it is not possible to directly demonstrate that this is true for *all* the higher modes $n \neq 1$.

4 The elastica compass and the elastica catapult

Once the rotation θ_l is computed from the non-linear equation (3.11) for a given load P and a clamp angle α , the rotation field $\theta(s)$ is obtained from integration of equation (3.4) as the solution of the equation

$$\cos^2 \left(\frac{\theta(s) + \alpha}{2} \right) = k^2 \text{Sn}^2[s\lambda + \mathcal{K}[\sigma_0, k], k], \quad (4.1)$$

With reference to the buckling load of the purely compressed clamped rod ($\alpha = \pi$), namely, $P_{cr} = \pi^2 B / (4l^2)$, the non-linear equation 3.11, considering only the first mode $n = 1$, can be rewritten as follows:

$$\frac{P}{P_{cr}} = \frac{4}{\pi^2} [\mathcal{K}(k) - \mathcal{K}(\sigma_0, k)]^2. \quad (4.2)$$

Equation (4.2) displays the two following different behaviours:

- when $P \leq P_{cr}$, a unique value of the rotation at the loaded end θ_l corresponds to a value of the clamp inclination α ;
- when $P > P_{cr}$, more than one solution for the rotation at the loaded end θ_l may exist when the clamp inclination α falls within the interval $(2\pi - \alpha_s, \alpha_s)$, with $\alpha_s \in [\pi, 2\pi]$.

These two behaviours are highlighted in Fig. 4.1, where the rotation (with respect to the vertical direction) $\theta_l + \alpha$ of the

loaded rod's end is reported as a function of the clamp inclination α , solution of the non-linear equation (4.2).

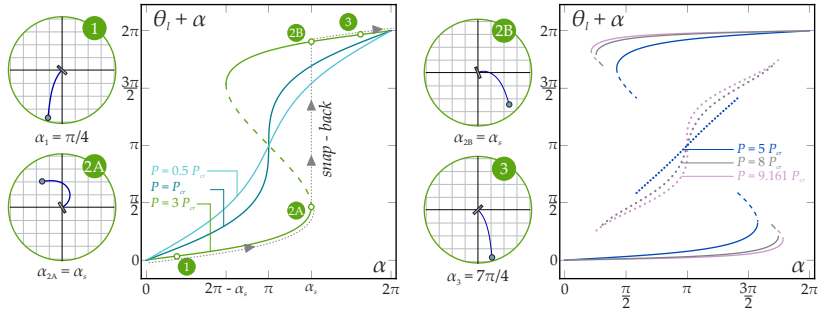


FIG. 4.1: Rotation of the loaded end of the rod $\theta_l + \alpha$ versus clamp angle α for different ratios P/P_{cr} , $\{0.5, 1, 3\}$ (left part) and $\{5, 8, 9.161\}$ (right part), showing the possibility of multiple equilibrium configurations (whenever $P > P_{cr}$) for sets of value of the clamp inclination α . Stable configurations are reported as continuous lines. Unstable equilibrium configurations associated to the first ($n = 1$) and second ($n = 2$) mode are reported as dashed and dotted lines, respectively. Deformed equilibrium configurations for the loading condition $P = 3P_{cr}$ are reported enclosed in green circles at different clamp rotations, when only one equilibrium configuration is possible ($\alpha_1 = \pi/4$ and $\alpha_3 = 7\pi/4$) and when two equilibrium configurations are possible ($\alpha_{2A} = \alpha_{2B} = \alpha_s = 1.348\pi$).

Six values of the ratio P/P_{cr} have been considered, namely, $\{0.5, 1, 3\}$ and $\{5, 8, 9.161\}$ in the left and right parts of Fig. 4.1, respectively. Uniqueness of the end rotation θ_l as a function of α is displayed only when the load P does not exceed the critical load P_{cr} (case $P = 0.5P_{cr}$), while more than one equilibrium configuration may be found when $P > P_{cr}$ for some set of values for the clamp angle α . For instance, in the case $P = 3P_{cr}$ (Fig. 4.1, left), three equilibrium configurations (related to $n = 1$) are displayed for the clamp angle α within the interval $(2\pi - \alpha_s, \alpha_s)$. Note that when the equilibrium configuration is not unique,

only two of the equilibrium configurations are stable (represented as continuous lines in the figure) while the others are unstable (represented as discontinuous lines). The limit case $P = P_{cr}$ (Fig. 4.1, left) is also reported, for which a vertical tangent is displayed at $\alpha = \pi$, which defines the transition between the two behaviours.

For completeness, it is observed that when $P \leq q^2 P_{cr}$ ($q \in \mathbb{N}$), the non-linear equation (4.2) may admit solutions for n -th mode, with $n < q$. For instance, when $P \in [9, 16]P_{cr}$, a total of five equilibrium configurations may exist for the same value of α (Fig. 4.1, right, case $P = 9.161P_{cr}$).

The uniqueness/non-uniqueness of the quasi-static solution defines two qualitatively different mechanical responses for the analysed elastic system. Indeed, considering a monotonic increase of the clamp angle α from 0 to 2π :

- when $P \leq P_{cr}$, the rotation θ_l changes continuously, so that the end of the rod describes a (smooth, convex and simple) closed continuous curve. In this condition the system behaves as an '*elastica compass*';
- when $P > P_{cr}$, the rotation θ_l reaches a critical value (corresponding to the snap clamp inclination $\alpha_s \in [\pi, 2\pi]$), for which a further increase in the clamp angle necessarily yields a jump in the rotation θ_l . Such a jump involves a release of elastic energy and a dynamic snap to another, non-adjacent configuration. In this condition the system behaves as an '*elastica catapult*'.

The clamp angle α_s for which the snap-back instability occurs has been numerically evaluated and is reported as a function of the load ratio P/P_{cr} in Fig. 4.2. It can be noted that α_s is always greater than π (limit value attained when P coincides with the buckling load, $P = P_{cr}$) and is an increasing function of the applied load, so that as the applied load increases

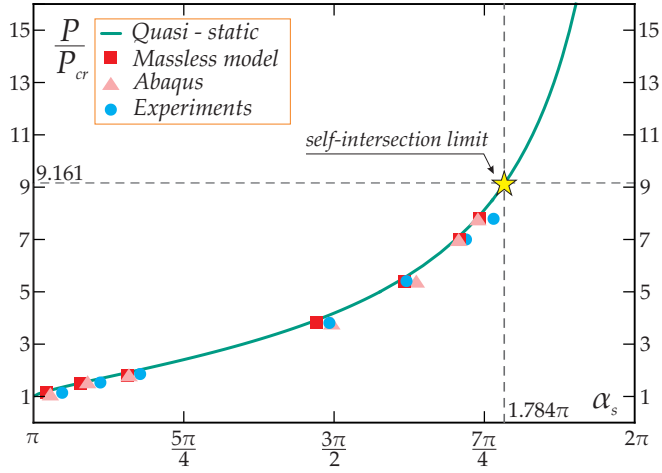


FIG. 4.2: Clamp inclination α_s , for which snap-back is attained, as a function of the load ratio P/P_{cr} . The theoretical prediction (continuous green line) is compared to the numerical evaluation (squares and triangles) obtained from the dynamic analysis (see Chapter 6) and the experimental data (circles) measured on the developed prototype (see Chapter 7).

the snap-back occurs 'later'. Results from the dynamic analyses (provided in Chapter 6) and from the experimental tests on the developed physical prototype (described in Chapter 7) are also reported in the figure. The agreement of the analytical predictions with the results obtained from experimental tests and the numerical simulations, taking into account of rod's inertia and extensibility, substantiates the assumptions (quasi-static conditions and rod's inextensibility) adopted in the analytical evaluation of the snap-back angle α_s .

4.0.1 Self intersection limit

In Fig. (4.2), the snap condition related to the load value P_{si} , defining the limit condition of self-intersection is highlighted.

It is found that, when $P = P_{si} \approx 9.161P_{cr}$, the deformed configuration displays a self-contact point with the clamp at the verge of the snap-back, $\alpha_s \approx 1.784\pi$. Therefore, the load P_{si} defines the lowest value of the load needed to achieve self-intersection of the elastic rod during rotation of the clamp.

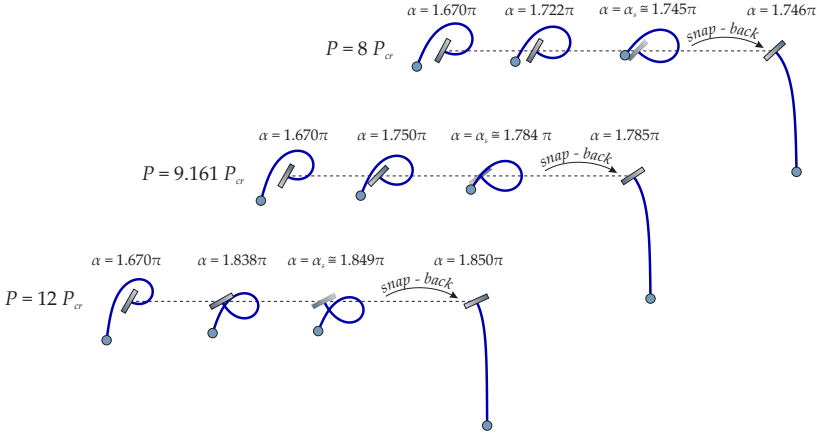


FIG. 4.3: A sequence of quasi-static configurations of the elastica catapult ($P/P_{cr} > 1$) at increasing the clamp angle α for different values of P/P_{cr} ending with snap in the equilibrium configuration. The self-intersection of the rod occurring for $P \geq P_{si}$ is displayed. In particular, the limit case of self-intersection is shown in the central sequence ($P = P_{si} \approx 9.161P_{cr}$) while self-intersection is shown in the lower sequence ($P = 12P_{cr}$).

Depending on the out-of-plane geometry of the rod, two behaviours can be attained in the case $P > P_{si}$:

- if the geometry permits self-intersection, the present solution holds and self-intersecting elastica are displayed,
- if the geometry does not permit self-intersection, a contact point is formed within the configuration of the rod at increasing the clamp rotation

4.1 The elastica compass

Considering a fixed weight P , the quasi-static evolution of the deformed configuration can be represented at varying the clamp angle α using the kinematical description (3.23). The trajectory travelled by the loaded end (playing the role of the pencil lead of the ‘elastica compass’) can be traced evaluating the coordinates (3.23) at the loaded end, $s = l$, at varying clamp inclination $\alpha \in [0, 2\pi]$. The quasi-static trajectories are reported in Fig. 4.4 for different values of the ratio P/P_{cr} .

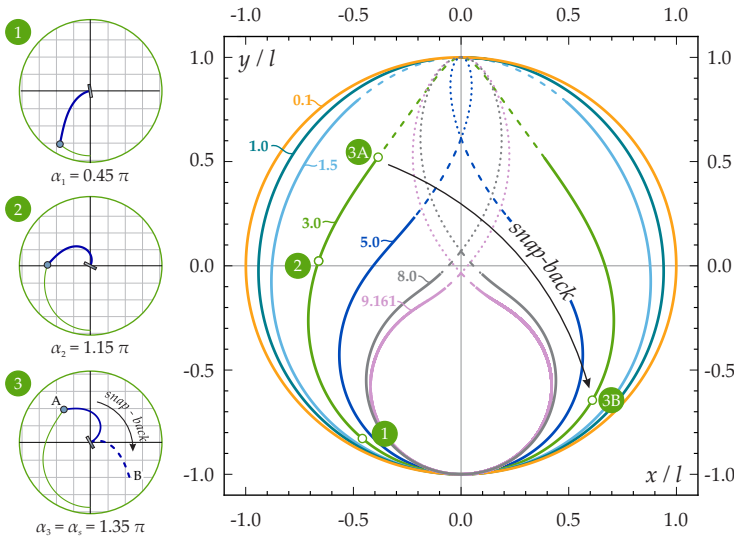


FIG. 4.4: ‘Pencil lead’ trajectories drawn by the elastica compass/catapult within the dimensionless plane x/l - y/l for different values of P/P_{cr} . Stable configurations are reported as continuous lines. Unstable positions are marked as discontinuous lines, dashed lines for the first mode and dotted lines for the second mode. Deformed configurations of the elastic rod for specific end positions are reported in the circles on the left for the case $P = 3P_{cr}$.

It can be observed that the trajectories have the shape of

4.1. The elastica compass

(smooth, convex and simple) closed curves in the case $P < P_{cr}$. Furthermore, unstable positions for the rod's end are reported as discontinuous line in the case $P > P_{cr}$ (as dashed and dotted line for the first and second mode configurations, respectively), so that the snap-back instability is initiated at the point where the continuous line ends.

The position of the loaded end can also be described in a polar reference system through the radius $r = \sqrt{x(l)^2 + y(l)^2}$ and the angle $\varphi = 3\pi/2 - \arctan [y(l)/x(l)]$, which result

$$\begin{cases} r = l\sqrt{A_1^2(l) + A_2^2(l)}, \\ \varphi = \frac{3\pi}{2} + \arctan\left(\frac{A_2(l)}{A_1(l)}\right). \end{cases} \quad (4.3)$$

The polar coordinates r (made dimensionless through division of the rod's length l) and φ which describe the rod's end trajectory are reported in Fig. 4.5 at varying the clamp angle α for different values of the ratio P/P_{cr} .

From Figs. 4.4 and 4.5 it can be observed that:

- the behaviour of the usual, namely, undeformable, compass is recovered in the limit of vanishing P/P_{cr} , for which the elastic rod behaves as a rigid bar, $r(\alpha) = l$ and $\varphi(\alpha) = \alpha$;
- due to the inextensibility assumption, the loops drawn by the elastica compass always lie inside the circle of radius l , therefore $r(\alpha) \leq l$;
- for dead loads smaller than the buckling load, $P < P_{cr}$, the loops drawn by the elastica compass are nearly circular despite the large difference between φ and α . This is due to the fact that the maximum percentage decrease in the radius length is about 6%;

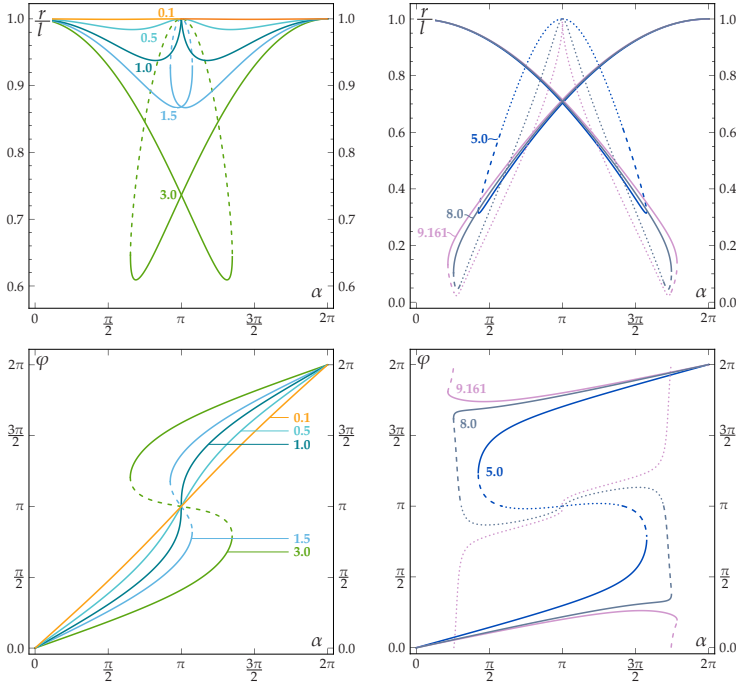


FIG. 4.5: ‘Pencil lead’ position of the elastica compass/catapult described in terms of the radius r (upper part) and the angle φ (lower part) as functions of the clamp angle α for different load ratios P/P_{cr} , $\{0.1, 0.5, 1, 1.5, 3\}$ (left part) and $\{5, 8, 9.161\}$ (right part). Unstable configurations are reported as discontinuous lines, dashed and dotted for first and second mode configurations, respectively.

- for dead loads larger than the buckling load, $P > P_{cr}$, the polar coordinate φ is limited by the upper bound $\varphi_{max}(P/P_{cr}) = \max_{\alpha} \varphi(\alpha, P/P_{cr})$, described by the dashed curve reported in Fig. 4.6 (left). Defining φ_s as the polar angle at the verge of the snap-back instability, namely $\varphi_s(P/P_{cr}) = \varphi(\alpha_s(P/P_{cr}), P/P_{cr})$ (reported as continuous curve), it is

4.1. The elastica compass

observed that $\varphi_s(P/P_{cr}) \leq \varphi_{max}(P/P_{cr})$, where the equality holds for $P/P_{cr} \leq 8.3$.

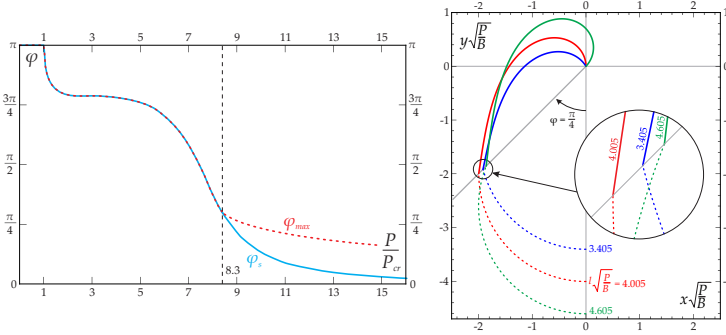


FIG. 4.6: Maximum polar angle φ_{max} (red/dashed line) and polar angle at the verge of the snap-back instability φ_s (blue/continuous line) as functions of the load ratio P/P_{cr} (left). The two polar angles coincide for the range $P/P_{cr} \leq 8.3$. Initial part of the trajectory (dashed lines) travelled by the loaded end of three soft robot arms reported within the dimensionless plane $x\sqrt{P/B}-y\sqrt{P/B}$. The three systems have the same bending stiffness B , are subject to the same weight P , but differ in the soft arm length, $l = \{3.405, 4.005, 4.605\}\sqrt{B/P}$ (right). The deformed configurations of the three systems are drawn (continuous line) for clamp inclinations $\alpha = \{0.826, 0.997, 1.239\}\pi$, respectively, for which the hanged load lies along the polar coordinate $\varphi = \pi/4$. The maximum radial distance r_{max} is attained with the system having the length $l = 4.005\sqrt{B/P}$.

In Fig. 4.6 (right), three soft robot arms with the same bending stiffness B , subject to the same weight P , but differing in the soft arm length, $l = \{3.405, 4.005, 4.605\}\sqrt{B/P}$ are considered. Deformed configurations (continuous line) are reported within the dimensionless plane $x\sqrt{P/B}-y\sqrt{P/B}$ at clamp inclinations $\alpha = \{0.826, 0.997, 1.239\}\pi$, for which the loaded ends of all the three systems have the same polar coordinate $\varphi = \pi/4$. The comparison of the radial coordinate of the loaded

ends for the three cases highlights that the maximum radial distance r_{max} corresponds to that of the system with arm length $l = 4.005\sqrt{B/P}$. This observation implies that lengthening of the arm does not always provide an increase in the attained distance. This concept is further analyzed in Chapter (5).

Finally, the quasi-static analysis is completed by the evaluation of the reaction moment at the rotating clamp $M(0) = -P x(l)$, which can be computed through the displacement field (3.23) as

$$M(0) = -A_1(l)Pl. \quad (4.4)$$

The reaction moment $M(0)$ is reported in Fig. 4.7, showing a change in sign at the snap-back, as a change in the sign of the rod's curvature occurs. This feature has been exploited to detect the snap inclination α_s from the results obtained with the numerical and experimental investigations explained in Chapters (6) and (7).

4.1. The elastica compass

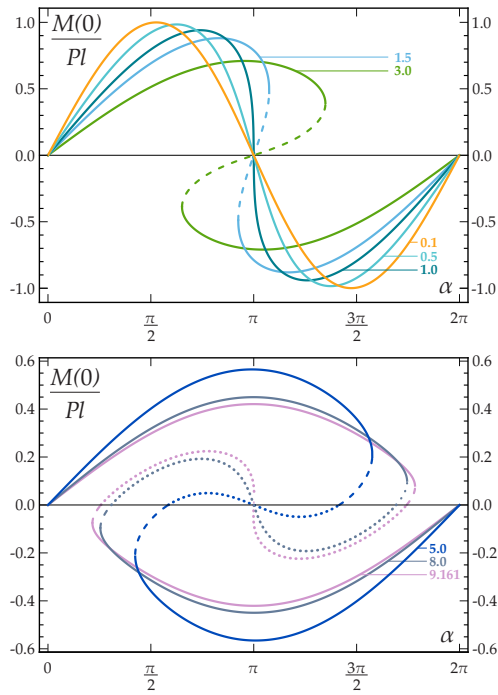


FIG. 4.7: Reaction moment $M(0)$ at the clamp at varying clamp angle α for different values of the load ratio P/P_{cr} equal to $\{0.1, 0.5, 1, 1.5, 3\}$ (upper part) and to $\{5, 8, 9.161\}$ (lower part). Moments evaluated at unstable configurations are reported as discontinuous lines, dashed and dotted for first and second mode configurations, respectively.

5 Robot's arm performance and design

The performances of the soft robot arm are investigated in terms of extremum distances that the loaded end can attain, which represent fundamental quantities in the design of soft robot arm, to achieve targeted positions for the hanged weight.

The maximum horizontal distance d_x , the maximum height d_y , and the minimum radial distance r_{min} reached by the hanged weight during the clamp rotation and before the possible snap-back instability, are introduced as

$$d_x = \max_{\alpha} \{-x(l)\}, \quad d_y = \max_{\alpha} \{y(l)\}, \quad r_{min} = \min_{\alpha} \{r\}, \quad (5.1)$$

where $\alpha \in [0, \pi]$ for the elastica compass ($P < P_{cr}$) and $\alpha \in [0, \alpha_s]$ for the elastica catapult ($P > P_{cr}$). Considering fixed both the length l and the stiffness B and exploiting the kinematical description (3.25), the distances d_x , d_y , r_{min} have been evaluated at varying load P and are reported in Fig. 5.1 (left), together with the respective clamp rotations α_x , α_y and α_r for which these distances are attained, Fig. 5.1 (right). The distance d_h (also called 'longest horizontal reach' by [39]) is defined as the horizontal distance attained by the weight when its vertical coordinate vanishes (namely, the weight and the clamp are at the same height):

$$d_h = -x(l), \quad \text{subject to the condition } y(l) = 0, \quad (5.2)$$

and has been evaluated and reported in Fig. 5.1, together with the respective angle α_h .

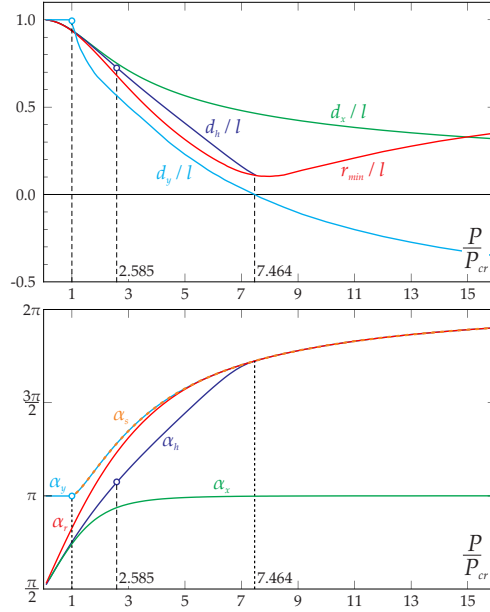


FIG. 5.1: Maximum horizontal distance d_x , maximum height d_y , and minimum radial distance r_{min} (upper part) and corresponding angles α_x , α_y , and α_r (lower part) plotted as functions of the load ratio P/P_{cr} . The distance d_h , equation (5.2), called 'longest horizontal reach' [39], the related angle α_h , and the snap angle curve α_s are also reported.

From Fig. 5.1, the following conclusions can be drawn at varying the load P and considering constant both the length l and the stiffness B .

- The maximum horizontal distance d_x attains its maximum value in the rigid limit ($P/P_{cr} = 0$), for which $d_x = l$, and is a decreasing function of the load P . The distance d_x is always attained for a clamp angle $\alpha_x \in [\pi/2, \pi]$.

- In the case of the elastica compass, the maximum height corresponds to the robot arm length, $d_y = l$, independently of the load $P \leq P_{cr}$ and is attained for $\alpha = \pi$. In the case of the elastica catapult, the maximum height d_y decreases at increasing load P and is attained at the verge of the snap-back instability, $\alpha_y = \alpha_s$. Moreover, when $P/P_{cr} > 7.464$, the weight always remains below the clamp before the occurrence of the snap-instability, $d_y < 0$. For such a load range, the longest reach d_h corresponds only to unstable configurations (and therefore cannot be attained).
- The minimum radial distance attains its minimum value $r_{min} = 0.104l$ for the load $P/P_{cr} = 7.985$. Moreover, when $P/P_{cr} > 5.665$ the minimum distance is achieved for a clamp rotation at the verge of instability ($\alpha_r = \alpha_s$).
- The distance d_h is always smaller than or equal to the horizontal distance d_x , namely $d_h \leq d_x$, where the equality holds only in the case of vanishing load, $P = 0$. Moreover, the distance d_h is defined only when $P/P_{cr} < 7.464$, because otherwise the configurations are unstable at null vertical coordinate, $y(l) = 0$.

It is worth to remark that the curves reported in Fig. 5.1 are plotted in a dimensionless plane, in which both axes are affected by a change in the rod length l . Therefore, playing with this length would permit to maximize the physical distances effectively reached by the loaded end when the hanged weight P is kept constant (as well as the bending stiffness B). Such maximum distances can be evaluated by seeking the load ratios P/P_{cr} for which the following function attains a maximum

$$\sqrt{\frac{P}{P_{cr}}} \frac{d_j(P/P_{cr})}{l}, \quad j = x, y, h. \quad (5.3)$$

The numerical implementation of this procedure leads to the following load ratios for which the soft arm displays the maximum possible distances

$$\left(\frac{P}{P_{cr}}\right)_{d_x^{max}} \rightarrow \infty, \quad \left(\frac{P}{P_{cr}}\right)_{d_y^{max}} = 1, \quad \left(\frac{P}{P_{cr}}\right)_{d_h^{max}} = 2.585. \quad (5.4)$$

The evaluated load ratios correspond to specific arm lengths l to be considered,

$$l = \frac{\pi}{2} \sqrt{\frac{P}{P_{cr}}} \sqrt{\frac{B}{P}}, \quad (5.5)$$

for achieving the maximum distances, namely

$$\frac{d_y}{l} = 1, \quad \frac{d_h}{l} = 0.726, \quad (5.6)$$

while the maximum distance d_x is represented by the trivial limit case of infinitely long arm, $l \rightarrow \infty$. The maximum distances d_y and d_h can be evaluated in terms of the hanged load P and the bending stiffness B as

$$\begin{aligned} d_y &= 1.571 \sqrt{\frac{B}{P}}, & \text{for } l &= 1.571 \sqrt{\frac{B}{P}}, \\ d_h &= 1.833 \sqrt{\frac{B}{P}}, & \text{for } l &= 2.525 \sqrt{\frac{B}{P}}, \end{aligned} \quad (5.7)$$

attained for the following clamp inclinations

$$\alpha_y = \pi, \quad \alpha_h = 1.072\pi. \quad (5.8)$$

The maximum distances d_y and d_h and related clamp inclination α_y and α_h are reported as spots in Fig. 5.1.

The optimization of the soft robot arm in terms of kinematics is completed by considering the maximum radial distance

$r_{max}(\varphi)$, defined as the maximization of the radial distance r for a given polar angle φ (keeping fixed the applied load P and the bending stiffness B). Following equation (5.3), the load ratio P/P_{cr} for which the maximum radial distance r_{max} is achieved can be found by seeking the maximum of the function

$$\sqrt{\frac{P}{P_{cr}}} \frac{r(P/P_{cr}, \varphi)}{l}. \quad (5.9)$$

Restricting the attention to the polar coordinate φ ranging between $\pi/4$ and π , the *optimal* load ratio P/P_{cr} has been reported in Fig. 5.2 (upper part, left) as the result of the maximization of equation (5.3). Under this loading condition, the maximum radial distance r_{max} (normalized through division by the length l) and the clamp inclination α (for which such a distance is attained) are evaluated at varying the angle φ in Fig. 5.2 (respectively, upper part, right, and lower part, left). Furthermore, the arm length l and the maximum radial distance r_{max} (made dimensionless through division by the constant parameters P and B) are provided in Fig. 5.2 (lower part, right).

It can be observed that:

- All the curves display a jump in their first derivative for the value $\varphi = 0.794\pi$. For polar coordinates φ higher than this value, the load ratio P/P_{cr} maximizing the radial distance corresponds to an angle equal to the maximum possible for that loading condition, $\varphi = \varphi_{max}$ (Fig. 5.2, upper part, left);
- The maximum radial distance is never observed for loads P smaller than the critical one P_{cr} and for clamp inclinations α smaller than π ;
- The results reported in Fig. 5.2 (lower part, right) represent an extension of the recent result by Wang [39] and Batista [1], referred to the case of an hanged load located

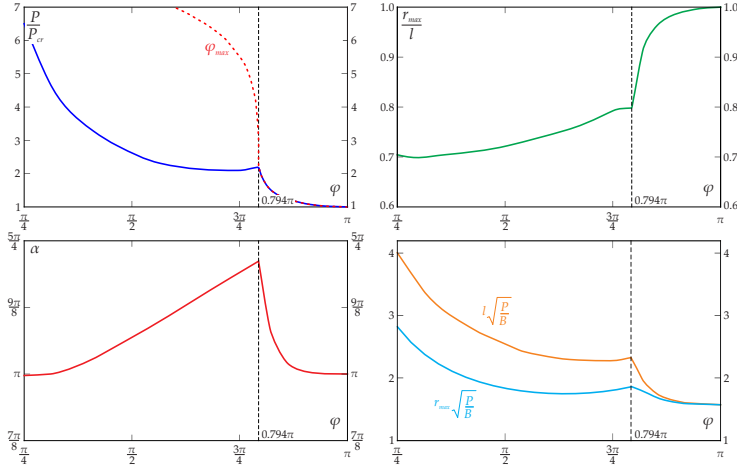


FIG. 5.2: Optimal load ratio P/P_{Cr} as a function of the polar coordinate φ for which equation (5.3) is maximized (upper part, left). Maximum radial distance r_{max} normalized through division by the length l (upper part, right) and corresponding clamp inclination α (lower part, left) as functions of the angle φ . Arm length l and the maximum radial distance r_{max} (made dimensionless through division by the fixed parameters P and B) at varying the polar angle φ (lower part, right).

along the horizontal axis x (at $\varphi = \pi/2$) and expressed by the distance d_h , see equation (5.7)₂. On the other hand, in the limit of $\varphi = \pi$, the value of the radial distance r_{max} approaches the value of the length l , see equation (5.7)₁.

- The curve reported in Fig. 5.2 (lower part, right) defines the values of the optimal lengths l for which the maximum radial distance is attained. In other words, lengthening does not always realize an increase in the achieved distances so that, using words similar to Wang [39], *shortening of rods may provide longer distances*, a key concept in the design of soft robot arms.

An applicative example of kinematic performance design towards the achievement of the maximum radial distance r_{max} , for given load P and stiffness B , is reported in Fig. 4.6 (right) for three soft robot arms differing only in their length. The deformed configurations, subject to the condition of loaded end lying along the polar coordinate $\varphi = \pi/4$, are shown for the three systems. It is observed that the maximum distance is attained when the soft arm has the optimal length $l = 4.005\sqrt{B/P}$, which value is provided by the curve reported in Fig. 5.2 (lower part, right) for $\varphi = \pi/4$.

Finally, with reference to the strength, the design of the arm cross section is ruled by the maximum bending moment M_{max} experienced along the elastic arm, $s \in [0, l]$, at varying the clamp inclination

$$M_{max} = \max_{\alpha, s \in [0, l]} M(s). \quad (5.10)$$

For the considered load range, $P/P_{cr} \in [0, 16]$, it is numerically found that the maximum bending moment always occurs at the clamp ($s = 0$) for the clamp inclination $\alpha = \alpha_x$, so that

$$M_{max} = Pd_x. \quad (5.11)$$

5.1 Energy release

In the case of the elastic catapult, when the clamp inclination approaches the value α_s , the snap-back instability induces a dynamic motion in the elastic system. Such a motion is due to the energy release of the system, provided in terms of the release of both elastic energy stored in the rod and the potential energy of the hanged load.

With reference to the two stable equilibrium configurations associated to the clamp rotation $\alpha \in [2\pi - \alpha_s, \alpha_s]$, the energy difference $\Delta\mathcal{E}$ can be computed as

$$\Delta\mathcal{E}(P, \alpha) = \frac{B}{2} \int_0^l \llbracket \theta'^2(s) \rrbracket ds + P \llbracket y(l) \rrbracket \quad (5.12)$$

where the symbol $\llbracket \cdot \rrbracket$ denotes the jump of the relevant argument evaluated for the configuration related to $\theta_l + \alpha \in [0, \pi]$ and for that related to $\theta_l + \alpha \in [\pi, 2\pi]$. Considering the kinematics at equilibrium, equations (2.1), (3.6)₁, and (3.23), the energy difference $\Delta\mathcal{E}$ (made dimensionless through division by B/l) can be re-written as

$$\frac{\Delta\mathcal{E}(P, \alpha) l}{B} = \llbracket 2A_1(l) + \cos(\theta_l + \alpha) \rrbracket \frac{\pi^2}{4} \frac{P}{P_{cr}}. \quad (5.13)$$

Because of symmetry of the paths in Fig. 4.1, the following relation for the energy difference holds

$$\Delta\mathcal{E}(P, 2\pi - \alpha) = -\Delta\mathcal{E}(P, \alpha), \quad \alpha \in [\pi, \alpha_s], \quad (5.14)$$

so that

$$\Delta\mathcal{E}(P, \alpha = \pi) = 0, \quad (5.15)$$

and therefore the clamp angle $\alpha = \pi$ represents the Maxwell line for the system [2], [30], [31].

The energy difference $\Delta\mathcal{E}(P, \alpha)$ is reported in Fig. 5.3 (left

5.1. Energy release

part) at varying the load ratio P/P_{cr} and the clamp angle $\alpha \in [\pi, \alpha_s]$. It is observed that the maximum energy difference, $\max_{\alpha} \Delta\mathcal{E}(P, \alpha)$ is attained at the verge of the snap instability, namely, at the clamp angle $\alpha = \alpha_s$.

Therefore, the energy release \mathcal{E}_R occurring at the snap-back, evaluated from the quasi-static solution, corresponds to the maximum energy difference possible for the elastic system,

$$\mathcal{E}_R(P) = \Delta\mathcal{E}(P, \alpha_s) \quad (5.16)$$

which is reported as a function of the applied load P in Fig. 5.3 (right part).

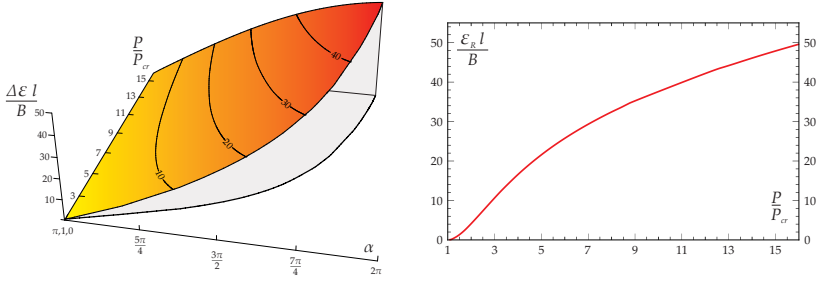


FIG. 5.3: Energy difference $\Delta\mathcal{E}$, equation (5.12), normalized through division by B/l , as a function of the load ratio P/P_{cr} and the clamp inclination α (left part). Energy release \mathcal{E}_R at snap-back ($\alpha = \alpha_s$), equation (5.16), as a function of the load ratio P/P_{cr} (right part).

6 Snap-back dynamics

The dynamics of the rotating cantilever rod, occurring as a consequence of the instability when the clamp is quasi-statically rotating, is here investigated through two models:

1. a simplified model (called ‘massless rod model’) where the rod’s inertia is neglected (because considered small when compared to the inertia of the point mass m) and regularizations are introduced through viscous damping due to air drag acting on the mass and axial compliance of the clamp constraint;
2. a finite element model (performed in Abaqus Ver 14.3), in which the inertia of the rod is fully accounted for and Rayleigh internal damping is present. A slightly different version of model (i.), which will be presented below, was proposed in the modelling of a tube-type manipulator arm by Snyder and Wilson [34].

It is shown that both models provide useful insights in the dynamics of the mechanical system after snap-back instability. However, while model 2 is capable to describe the complete dynamic evolution of the system up to a wide range of loading parameters, the model 1 can predict the full dynamics only until deformation modes higher than the first do not enter the solution (in other words, the massless rod model works correctly for P/P_{cr} smaller than ≈ 2).

6.1 Massless rod model

In the model where the rod's mass γ (as well as any rotational inertia) is neglected, the dynamics of the whole system is characterized only by the translational inertia of the lumped mass m at the rod's free end.

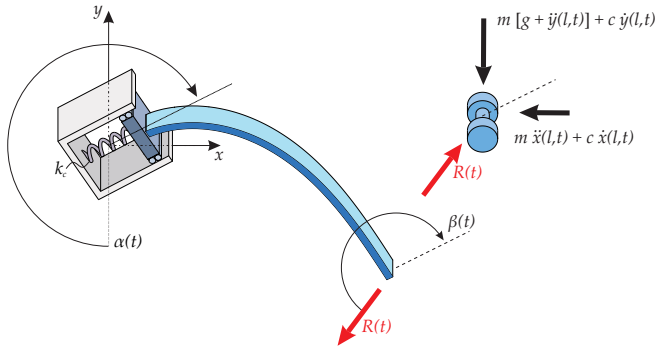


FIG. 6.1: Free-body diagram of the massless rod model: schemes of the massless elastic rod (left) and the lumped mass (right). Regularization of the solution obtained with this simplified model is achieved through the introduction of the viscous coefficient c due to air drag and the finite stiffness k_c of the clamp.

Within a dynamic framework, the force resultant acting at the free end, $R(t)$, has an inclination angle $\beta(t)$ with respect to the (straight) undeformed configuration (see Fig. 6.1)

$$R(t) = \sqrt{R_x(t)^2 + R_y(t)^2},$$

$$\beta(t) = \alpha(t) + \arctan \frac{R_x(t)}{R_y(t)}. \quad (6.1)$$

The differential system governing the dynamic behaviour of such a system is obtained imposing the II Newton's law on the mass, namely, that the components $R_x(t)$ and $R_y(t)$ of the

6.1. Massless rod model

resultant $R(t)$

$$\begin{aligned} R_x(t) &= -R(t) \sin[\alpha(t) - \beta(t)], \\ R_y(t) &= -R(t) \cos[\alpha(t) - \beta(t)], \end{aligned} \quad (6.2)$$

should be given as the sum of the respective translational inertia, the (linear) viscous damping force, and the dead load

$$\begin{aligned} R_x(t) &= -m\ddot{x}(l, t) - c\dot{x}(l, t), \\ R_y(t) &= -m[g + \ddot{y}(l, t)] - c\dot{y}(l, t), \end{aligned} \quad (6.3)$$

where c is the damping coefficient due to air drag.

Introducing the reference time $T = \sqrt{ml^3/B}$ and the following dimensionless quantities

$$\begin{aligned} \tau &= \frac{t}{T}, \quad \xi(\tau) = \frac{x(l, t)}{l}, \quad \eta(\tau) = \frac{y(l, t)}{l}, \\ \mu(\tau) &= \frac{R(t) l^2}{B}, \quad \kappa_c = \frac{kc l^3}{B}, \quad v = c \sqrt{\frac{l^3}{mB}}, \quad \zeta = \frac{gml^2}{B}, \end{aligned} \quad (6.4)$$

a comparison of equations (6.2) with the differential equations (6.3) leads to the following non-dimensionalized differential system, governing the snap-back dynamics

$$\begin{cases} \frac{d^2 \xi(\tau)}{d\tau^2} + v \frac{d\xi(\tau)}{d\tau} = \mu(\tau) \sin[\alpha(\tau) - \beta(\tau)], \\ \frac{d^2 \eta(\tau)}{d\tau^2} + v \frac{d\eta(\tau)}{d\tau} + \zeta = \mu(\tau) \cos[\alpha(\tau) - \beta(\tau)]. \end{cases} \quad (6.5)$$

The rotation field of the rod's axis is governed by the elastica

$$\theta''(s, \tau) - \mu(t) \sin[\theta(s, \tau) + \beta(\tau)] = 0, \quad (6.6)$$

that is the same as for the quasi-static problem (3.3), but with the two functions of time $\mu(\tau)$ and $\beta(\tau)$ replacing now P and α , respectively. Therefore, the integration in space for the dynamic problem, equation (6.6), can be computed similarly to the quasi-static case (Chapter 3) restricted to the first deformation mode, $n = 1$. This integration yields the following relation between the normalized resultant $\mu(\tau)$, the rotation of the rod at the free end $\theta(l, \tau)$, and the resultant inclination $\beta(\tau)$

$$\mu(\tau) = [\mathcal{K}(h(\tau)) - \mathcal{K}(\chi_0(\tau), h(\tau))]^2, \quad (6.7)$$

where

$$\begin{aligned} h^2(\tau) &= \cos^2 \left(\frac{\theta(l, \tau) + \beta(\tau)}{2} \right), \\ \chi_0(\tau) &= -\arcsin \left[\frac{1}{h(\tau)} \cos \left(\frac{\beta(\tau)}{2} \right) \right]. \end{aligned} \quad (6.8)$$

On the other hand, the normalized displacements at the free end, $\xi(\tau)$ and $\eta(\tau)$, follow from the displacement field for the quasi-static problem, equation (3.25), considering now the axial compliance of the system (neglected in the quasi-static calculations) introducing an axial spring of stiffness k_c in the clamp,

$$\begin{aligned}
 \zeta(\tau) &= -\frac{\mu(\tau) \cos \beta(\tau) \cos \alpha(\tau)}{\kappa_c} + \\
 &\quad -\frac{2h(\tau)}{\sqrt{\mu(\tau)}} \left\{ \text{Cn} \left[\sqrt{\mu(\tau)} + K(\chi_0(\tau), h(\tau)), h(\tau) \right] + \right. \\
 &\quad \left. -\text{Cn} [\mathcal{K}(\chi_0(\tau), h(\tau)), h(\tau)] \right\}, \\
 \eta(\tau) &= -1 - \frac{\mu(\tau) \cos \beta(\tau) \sin \alpha(\tau)}{\kappa_c} + \\
 &\quad + \frac{2}{\sqrt{\mu(\tau)}} \left\{ E \left[\text{am} \left(\sqrt{\mu(\tau)} + K(\chi_0(\tau), h(\tau)), h(\tau) \right) \right] + \right. \\
 &\quad \left. -E [\mathcal{K}(\chi_0(\tau), h(\tau)), h(\tau)] \right\}.
 \end{aligned} \tag{6.9}$$

The substitution of the expressions (6.7) and (6.9) for $\mu(\tau)$, $\zeta(\tau)$, $\eta(\tau)$ in the differential equations (6.5) leads to a non-linear second-order differential implicit system for the evolution of the free end rotation $\theta_l(\tau)$ and for the resultant inclination $\beta(\tau)$. For given initial conditions and rotation law $\alpha(\tau)$, the integration of the differential system (6.5) can finally be numerically performed.

Initial conditions

In the present analysis, initial rest condition for the system and a linear time evolution law for the clamp rotation are considered, so that

$$\alpha(t) = \alpha_0 + \omega t, \tag{6.10}$$

where α_0 is the initial clamp rotation and ω is the clamp angular velocity, and which can be rewritten in terms of dimensionless time as

$$\alpha(\tau) = \alpha_0 + \Omega \tau, \quad (6.11)$$

with Ω being the clamp angular velocity referred to the dimensionless time,

$$\Omega = \omega T. \quad (6.12)$$

To avoid a trivial solution, the evolution of the system was analysed starting at $\tau = 0$ from an ‘almost’ undeformed state for the rod, namely, the initial clamp inclination was set to be $\alpha_0 = 10^{-5}$.

The rest condition for the system at $\tau = 0$ implies that initially the inclination $\beta(0)$ coincides with the clamp inclination $\alpha(0)$, so that the force resultant $R(0)$ momentarily coincides with the dead load P , and that the lumped mass has null velocity,

$$\beta(0) = \alpha(0), \quad \mu(0) = \zeta, \quad \dot{\zeta}(0) = \dot{\eta}(0) = 0. \quad (6.13)$$

The four conditions (6.13) imply four initial conditions for the resultant inclination $\beta(\tau)$ and the free end rotation $\theta(l, \tau)$,

$$\beta(0) = \alpha_0, \quad \theta_l(, 0) = \theta_{l0}, \quad \dot{\beta}(0) = \dot{\beta}_0, \quad \dot{\theta}_l(0) = \dot{\theta}_{l0}, \quad (6.14)$$

where the values of θ_{l0} , $\dot{\beta}_0$, and $\dot{\theta}_{l0}$ can be computed using equation (6.7) and equation (6.9).

The evolution of the resultant inclination $\beta(\tau)$ and the free end rotation $\theta(l, \tau)$ are obtained from the numerical integration of the non-linear differential implicit equations (6.5) through the function `NDSolve` in Mathematica[©] (ver. 10). Considering the clamp angular velocity $\omega = 0.014$ rad/s and assuming a small normalized damping coefficient $v = 0.069$ and high normalized axial stiffness $\kappa_c = 310$, the numerical integration

has been performed at varying the normalized mass parameter, namely for $\zeta = \{1.157, 1.987, 2.818, 3.648, 4.478\}$ corresponding to $P/P_{cr} = \{0.469, 0.805, 1.142, 1.479, 1.815\}$ and which are representative of some of the experimental set-ups considered in Chapter 7.

The massless model is able to capture reasonably well the dynamics of the system for values of the normalized mass parameter ζ lower than 5, corresponding to $P/P_{cr} < 2$. For higher values of ζ , the numerical integration fails to converge soon after the snap-back instability occurs, namely, the free end experiences a very fast and large oscillation in its acceleration, and the Mathematica solver reveals that the differential system becomes stiff. The encountered difficulty in the numerical treatment is related to the fact that rod configuration is imposed to assume the first quasi-static mode during the dynamics, a condition which becomes not representative at values $P/P_{cr} > 2$. Indeed, it is experimentally shown in Chapter 7 that for this loading condition the dynamics of the rod is characterized by both transverse and longitudinal oscillation, while the present simplified model is reliable only when transverse oscillations prevail in the dynamic response.

6.2 Finite element analysis

A finite element analysis of the system was performed in Abaqus with the purpose to provide a full description of the dynamics of the rod for every loading condition, thus overcoming the limitations found with the simplified model. The rod is modelled through 100 linear elastic planar beam elements, where the first element has the external edge constrained by the rotating clamp while the lumped mass m is attached on the external edge of the final element. Introducing energy dissipation through Rayleigh damping, large displacement analysis were performed through the following two steps:

- Static – The gravitational force is applied in order to establish the deformed initial configuration. Here a quasi-static deformation is produced by the weight of both the elastic rod and the lumped mass (although the effect of the former is much smaller than the effect induced by the latter);
- Dynamic implicit – A slow rotation to the clamped end is imposed as a boundary condition. The analysis takes into account the inertial forces generated during the clamp rotation.

Simulations were run considering geometry, material, inertia and clamp angular velocity representative of the experimental set-up described in the next Chapter. Rayleigh damping was set through the mass-proportional damping coefficient $A = 10^{-2} \text{ s}^{-1}$ and the stiffness-proportional damping coefficient $B = 5 \times 10^{-3} \text{ s}$. Several low rotation velocities for the clamp have been investigated ($\omega = \{0.014, 0.06, 0.14\} \text{ rad/sec}$), basically showing no influence of small ω on the dynamics of the system.

7 Experiments vs modelling

An experimental setup was designed and manufactured at the Instabilities Lab of the University of Trento for the analysis of the rotating clamped elastic rod (Fig. 7.1). A rack and pinion actuator (Fig. 7.1c) was used to transform the linear motion of an electromechanical testing machine (ELE Tritest 50 from ELE International Ltd) into the rotation of the clamp at required angular speeds (different low clamp velocities were tested in the experiments, without noting substantial differences, so that only results for $\omega = 0.014$ rad/sec are reported). The angular position of the rotating clamp was measured through a contactless rotary position sensor (NRH280DP/180/360). The moment transmitted to the clamp was measured with a lever system connected to a load cell (Leane DBBSN, RC 10kg), as evident from Fig. 7.1c.

During the tests, the modulus of the acceleration of the lumped mass, attached at the end of the beam

$$a(l, t) = \sqrt{\dot{x}(l, t)^2 + \dot{y}(l, t)^2} \quad (7.1)$$

was obtained mounting two miniaturized mono-axial accelerometers (352A24, PCB piezotronics, 0.8 grams) perpendicular to each other. All the data were acquired with a NI compactRIO system interfaced with Labview 2013 (from National Instruments).

Two rods were used, both made up of a solid polycarbonate strip (white 2099 Makrolon UV from Bayer, $E = 2350$ MPa, Poisson's ratio $\nu = 0.37$ and volumetric mass density $\rho = 1180$ kg/m³). One rod, 345 mm long, has a 25×3 mm cross section and the other, 700 mm long, has a 25×2.85 mm cross section. The masses attached at the end of the two rods were chosen to produce the following values of $P/P_{cr} = \{0.469, 0.805, 1.142, 1.479, 1.815, 3.813, 5.405, 6.998, 7.795\}$.

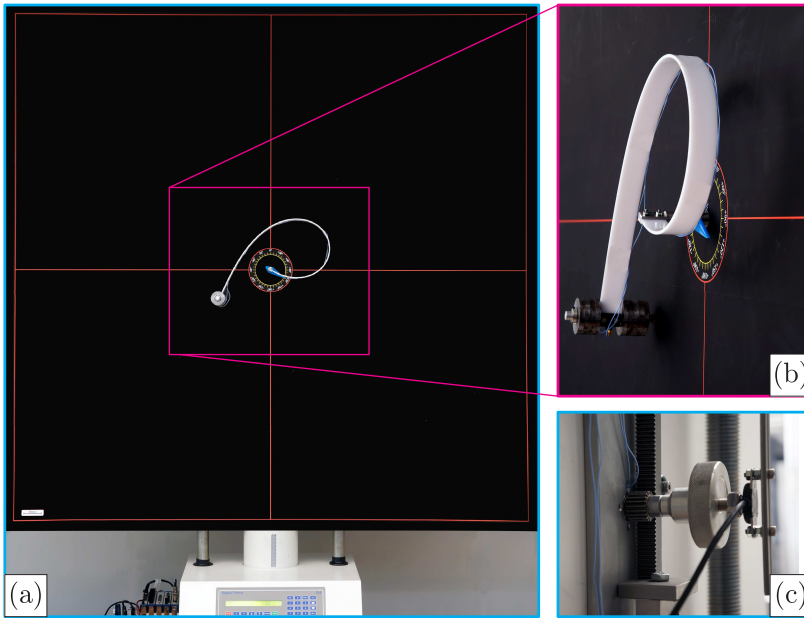


FIG. 7.1: Experimental setup for the elastica compass and the elastica catapult. (a) Global view of the experimental setup, (b) detail of the elastic rod, and (c) rear view detail of the rack and pinion mechanism to impose clamp rotation and from which the rotary position sensor is visible.

Results of experiments are shown in Figs. 4.2, 7.2, 7.3, and

7.4. In particular, in Fig. 4.2 the experimental points corresponding to the snap angles have been recorded from a change in sign of the moment measured at the clamp. The same moment $M(0)$ is reported in Figs. 7.2 and 7.3 as a function of the clamp rotation α for the case of the elastica compass ($P/P_{cr} = 0.805$, where a quasi-static path is followed, Fig. 7.2) and in the case of the elastica catapult ($P/P_{cr} = 1.142$ and $P/P_{cr} = 7.795$, where the dynamics prevails after snap-back, Fig. 7.3 upper part on the left and on the right, respectively). In the case of the elastica compass the acceleration $a(l, t)$ was found to be negligible (the maximum value was about 10^{-2} g), while in the case of the elastica catapult the acceleration $a(l, t)$ (reported in Fig. 7.3, lower part) was found to have a peak of about 0.6g and 55g for $P/P_{cr} = 1.142$ and $P/P_{cr} = 7.795$, respectively. These peaks in the acceleration were found to occur just after the snap-back instability.

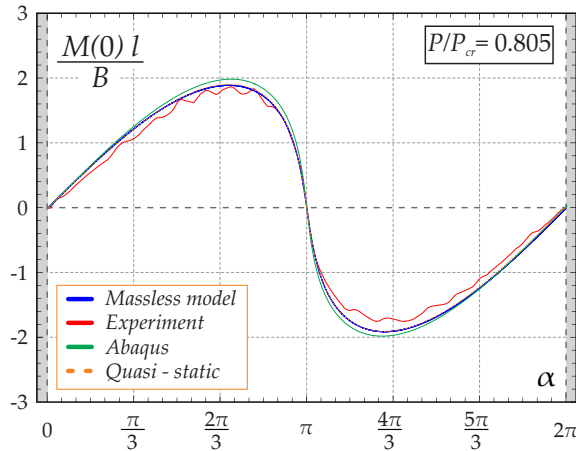


FIG. 7.2: Comparison between the theoretically predicted and experimentally measured values of the moment at the clamp $M(0)$ at varying the clamp angle α for the elastica compass, in the case $P = 0.805P_{cr}$.

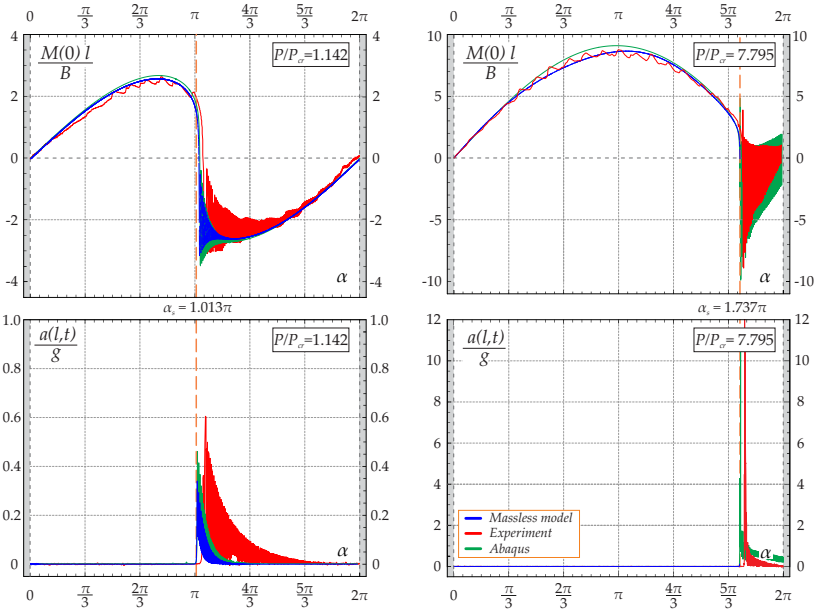


FIG. 7.3: Comparison between the theoretically predicted and experimentally measured values of the moment at the clamp $M(0)$ (upper part) and of the total acceleration of the lumped mass $a(l,t) = \sqrt{\ddot{x}(l,t)^2 + \ddot{y}(l,t)^2}$ (lower part) at varying the clamp angle α for the elastica catapult in the cases $P = 1.142P_{cr}$ (left column) and $P = 7.795P_{cr}$ (right column). The curves highlight the presence of snap-back dynamics during the clamp rotation when the angle α_s is approached. In particular, a change in sign for the moment at the clamp $M(0)$ is observed as well as high acceleration of the rod's end after the snap-back phenomena.

Photos taken at different rotation angles are superimposed in Fig. 7.4 for two cases in which the system behaves as an elastica compass (figure a, $P/P_{cr} = 0.805$) and an elastica catapult (figure b, $P/P_{cr} = 7.795$). In the latter case, the photo labelled 12 corresponds to the last photo taken before snap-back instability ($\alpha = 1.744\pi$), while photos 13 and 14 are blurred because

they were taken (using a NEX-5N Sony camera) during post-snap dynamics. Note that the shutter speed was set on $1/20$ s, which provides a measure of the velocity of the rod during snap-back. In Fig. 7.4, the position of the attached lumped mass is compared with the theoretically predicted rod's end trajectory (two theoretical predictions are reported, one for quasi-static behaviour, yellow line, and the other for dynamic motion with the massless model, dashed green line), showing a very nice agreement.

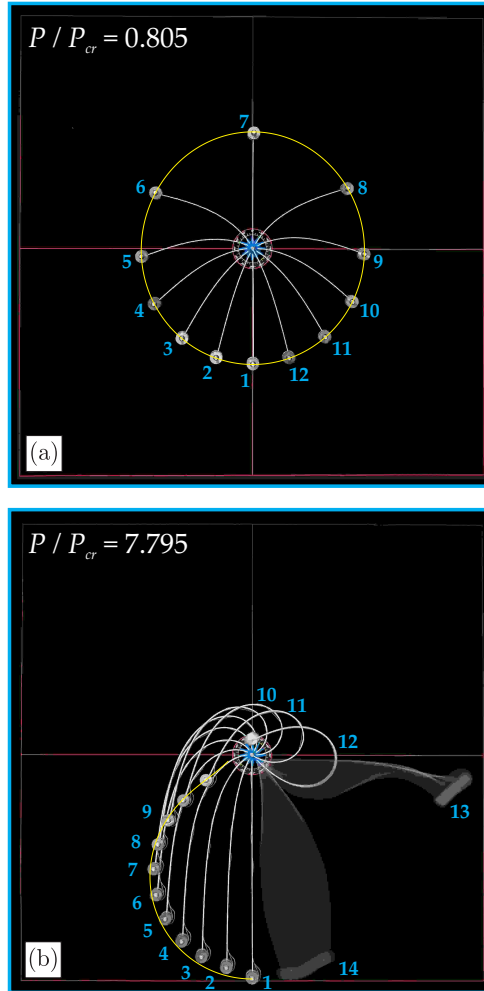


FIG. 7.4: Superimposed photos at different clamp angles α for (a) the elastica compass, $P/P_{cr} = 0.805$, and (b) the elastica catapult, $P/P_{cr} = 7.795$. The blurred images in the photo on the right were taken during the post-snap dynamics at $1/20$ s shutter speed. The theoretical trajectory of the ‘pencil lead’, obtained from the quasi-static analysis, is reported as continuous yellow line.

8 Conclusions and main scientific output

In the simplest set-up for a flexible robot arm, an elastic rod is subject to a prescribed slow rotation at one end and to a concentrated mass in a gravity field at the other. Solving this system through the elastica has evidenced a discriminating role for the applied load. When the load is smaller than the buckling load (for the straight configuration), the loaded end describes a closed continuous curve (not far from an ellipse), while when it is higher the continuous displacement of the loaded end terminates in an unstable geometrical form, from which a snap-back instability leads to a non-adjacent configuration. In the former case the system behaves as an 'elastica compass' (so that the loaded end of the arm would describe a circle if the rod would be rigid), while in the latter case the system behaves as an 'elastica catapult' (so that the mass would be thrown away if detachment would be allowed). The dynamic motion after the snap instability has been analyzed with a standard finite element program and an *ad hoc* developed software. The quasi-static and dynamical behaviours have been validated with a specifically designed experimental set-up. Results show that the basic problem of soft robot arm addressed in the present thesis, and systematically explored in terms of mechanical performances, can be analytically and numerically described with a great accuracy and therefore is ready to exploitation in real devices.

The main results presented in the first part of the thesis have

Chapter 8. Conclusions and main scientific output

been summarised in the paper C. Armanini, F. Dal Corso, D. Misseroni and D. Bigoni, "From the elastica compass to the elastica catapult: an essay on the mechanics of soft robot arm". In: *Proceedings of the Royal Society A*, (2017), **473**,20160870. Cover paper.

Part II

Configurational forces within a dynamic framework

9 Introduction

Configurational forces were introduced by Eshelby to explain the motion, induced by mechanical or thermal loadings, of defects within a solid body towards the achievement of an equilibrium configuration [12] [13] [14] and [15]. When movable constraints are considered in a structural system, similar forces are generated, noticeable affecting the overall mechanical response ([4],[6]). The second part of this thesis is devoted to proving the action of configurational forces on structural systems within a dynamical framework.

A rod is considered constrained on one end by a frictionless sliding sleeve with an inclination angle α and subject at the other end to a dead load given by a lumped mass. From the undeformed (rectilinear) configuration, the rod is suddenly released and a dynamic motion initiates due to the gravitational field. During the motion, the length of the rod within the sliding sleeve varies. Such a length represents a configurational parameter for the system and, through a variational approach, a configurational force is proven to be generated at the exit of the sliding constraint. In particular, it is found that this force coincides with that predicted within the quasi-static framework, extending previous analysis [3].

Inspired by the massless rod model conceived for the snap-back dynamics of the elastic catapult described in **Part I** (Chapter 6), a numerical procedure is introduced to fully describe the dynamical response of the system occurring after the sudden release. A critical value of the dimensionless load parameter

p , condensing both the values of the lumped mass, rod stiffness and rod' initial length, is found as a function of the sliding sleeve inclination α , for which a transition between two different behaviours occur. The two behaviours are characterized by two opposite final stages, where the rod is finally injected or finally ejected. Two specific sets of pairs of dimensionless load p and sliding sleeve inclination α are found to define the two possible final stages. The theoretical results are fully validated through experimental tests on a specific set-up realised at the Instabilities Lab of the University of Trento.

10 Formulation

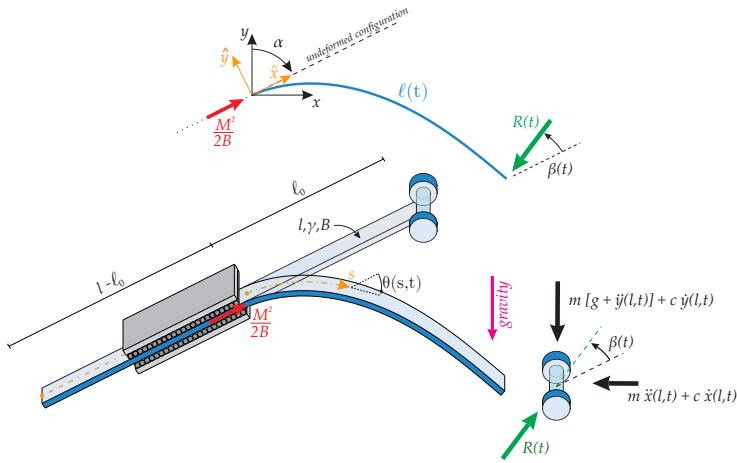


FIG. 10.1: An inextensible rod of total length l , bending stiffness B and linear mass density γ is constrained by a frictionless sliding sleeve inclined by an angle α . A lumped mass m is attached at the other end of the rod, providing a weight $P = mg$. The part of the rod outside the sliding sleeve is measured through $l(t)$, with $l_0 = l(t = 0)$ representing the length at the initial time $t = 0$. The rotation of the rod's axis with respect to the undeformed straight configuration is measured through the rotation field $\theta(s, t)$, with s being the curvilinear coordinate, $s \in [0, l]$. The reference systems $\hat{x} - \hat{y}$ and $x - y$ are reported, both centered at the exit of the sliding sleeve. The configurational force $M^2/2B$ is realized at the exit of the sliding sleeve.

10.1 Kinematics

The kinematics of an inextensible elastic rod of length l , rectilinear in its undeformed configuration, is described in the time variable t and within the plane $x - y$ through the curvilinear coordinate $s \in [0, l]$. The primary kinematic field for the elastic rod is the rotation $\theta(s, t)$, measuring the clockwise angle with respect to the undeformed state, and from which the position field can be evaluated, considering the inextensibility constraint, as

$$\begin{aligned} x(s, t) &= x(0, t) + \int_0^s \sin [\theta(s, t) + \alpha] ds, \\ y(s, t) &= y(0, t) + \int_0^s \cos [\theta(s, t) + \alpha] ds. \end{aligned} \quad (10.1)$$

A frictionless sliding sleeve, with exit point centered at the coordinate $\{x = y = 0\}$ and inclined by an angle α with respect to the y axis, is constraining the rod. The considered system is therefore characterized by the configurational parameter $\ell(t) \in [0, l]$ measuring the length of rod outside the constraint, $s \in [l - \ell(t), l]$. It follows that the sliding sleeve provides the following kinematic constraint for value of the position field at the curvilinear coordinate $s = l - \ell(t)$

$$x(l - \ell(t), t) = y(l - \ell(t), t) = 0, \quad (10.2)$$

and the rotation for the part of rod within the sliding sleeve

$$\theta(s, t) = 0 \quad s \in [0, l - \ell(t)], \quad (10.3)$$

so that the position fields $x(s, t)$ and $y(s, t)$, equations (10.1), reduce to

$$x(s, t) = \begin{cases} -(l - \ell(t) - s) \sin \alpha, & s \in [0, l - \ell(t)], \\ \int_{l - \ell(t)}^s \sin [\theta(s, t) + \alpha] ds, & s \in [l - \ell(t), l], \end{cases} \quad (10.4)$$

$$y(s, t) = \begin{cases} -(l - \ell(t) - s) \cos \alpha, & s \in [0, l - \ell(t)], \\ \int_{l - \ell(t)}^s \cos [\theta(s, t) + \alpha] ds, & s \in [l - \ell(t), l]. \end{cases} \quad (10.5)$$

A further reference system $\hat{x} - \hat{y}$ is considered, obtained as the counter-clockwise rotation of the system $x - y$ by the angle $\pi/2 - \alpha$, namely with the \hat{x} axis parallel to the sliding direction:

$$\begin{Bmatrix} \hat{x}(s, t) \\ \hat{y}(s, t) \end{Bmatrix} = \begin{bmatrix} \sin \alpha & \cos \alpha \\ -\cos \alpha & \sin \alpha \end{bmatrix} \begin{Bmatrix} x(s, t) \\ y(s, t) \end{Bmatrix}. \quad (10.6)$$

Within this reference system, the rod's kinematics can be described through the coordinates $\hat{x}(s, t)$ and $\hat{y}(s, t)$ as

$$\begin{aligned} \hat{x}(s, t) &= \hat{x}(0, t) + \int_0^s \cos \theta(s, t) ds, \\ \hat{y}(s, t) &= \hat{y}(0, t) - \int_0^s \sin \theta(s, t) ds \end{aligned} \quad (10.7)$$

so that equations (10.2) imply

$$\hat{x}(s = l - \ell(t), t) = \hat{y}(s = l - \ell(t), t) = 0, \quad (10.8)$$

and, from equations (10.4) and (10.5), the position fields $\hat{x}(s, t)$ and $\hat{y}(s, t)$ become

$$\widehat{x}(s, t) = \begin{cases} -(l - \ell(t) - s) & s \in [0, l - \ell(t)], \\ \int_{l - \ell(t)}^s \cos \theta(s, t) ds, & s \in [l - \ell(t), l], \end{cases} \quad (10.9)$$

$$\widehat{y}(s, t) = \begin{cases} 0, & s \in [0, l - \ell(t)], \\ - \int_{l - \ell(t)}^s \sin \theta(s, t) ds, & s \in [l - \ell(t), l]. \end{cases} \quad (10.10)$$

From the kinematics it follows that the velocity fields $\dot{x}(s, t)$ and $\dot{y}(s, t)$ (where a dot represents the time derivative) for the part of rod within the sliding sleeve are given by

$$\begin{cases} \dot{x}(s, t) = \dot{\ell}(t) \sin \alpha, \\ \dot{y}(s, t) = \dot{\ell}(t) \cos \alpha, \end{cases} \quad s \in [0, l - \ell(t)], \quad (10.11)$$

or, equivalently

$$\begin{cases} \dot{\widehat{x}}(s, t) = \dot{\ell}(t), \\ \dot{\widehat{y}}(s, t) = 0, \end{cases} \quad s \in [0, l - \ell(t)]. \quad (10.12)$$

10.2 Lagrangian and governing equations from variational approach

The Lagrangian functional $\mathcal{L}(t)$ for the considered system is given by

$$\begin{aligned} \mathcal{L}(t) = & \mathcal{T}(t) - \mathcal{V}(t) + \\ & - \int_0^l N_x(s, t) \{x'(s, t) - \sin[\theta(s, t) + \alpha]\} ds + \\ & - \int_0^l N_y(s, t) \{y'(s, t) - \cos[\theta(s, t) + \alpha]\} ds, \end{aligned} \quad (10.13)$$

where $N_x(s)$ and $N_y(s)$ are Lagrangian multipliers (representing the internal forces along the x and y directions). Considering that the elastic system has uniform distributed mass γ and is bearing an external lumped mass m at the coordinate $s = l$, neglecting the rotational inertia for both the rod and the external mass, the kinetic energy $\mathcal{T}(t)$ of the system is given by

$$\begin{aligned} \mathcal{T}(t) = & \frac{m[\dot{x}^2(l, t) + \dot{y}^2(l, t)]}{2} + \\ & + \frac{1}{2} \int_0^l \gamma[\dot{x}^2(s, t) + \dot{y}^2(s, t)] ds. \end{aligned} \quad (10.14)$$

The functional $\mathcal{V}(t)$ represents the potential energy given as the sum of the elastic energy stored within the rod and the negative of the work done by the loads applied to the system. A quadratic form in the curvature is assumed for the strain energy of the elastic rod, so that the moment at the coordinate s is given by $M(s, t) = B\theta'(s, t)$ where B is the bending stiffness. Considering a gravitational field characterized by the acceleration g in direction opposite to the y axis, the concentrated dead

load $P = mg$ is applied at the coordinate $s = l$ while the uniform dead load γg is distributed all along the rod.

$$\mathcal{V}(t) = \frac{B}{2} \int_{l-\ell(t)}^l \theta'(s,t)^2 ds + Py(l,t) + \int_0^l \gamma gy(s,t) ds. \quad (10.15)$$

Finally, the principle of least action can be applied to the functional \mathcal{A} defined as the integration in time of $\mathcal{L}(t)$

$$\mathcal{A} = \int_{t_0}^{t^*} \mathcal{L}(t) dt, \quad (10.16)$$

with t_0 and t^* being arbitrary initial and final instants of the analyzed time interval.

To perform the minimization of the functional \mathcal{A} , the kinematic fields $\{x(s,t), y(s,t), \theta(s,t)\}$, and the configurational parameter $\ell(t)$ are respectively perturbed by the variation fields $\{\epsilon x_{var}(s,t), \epsilon y_{var}(s,t), \epsilon \theta_{var}(s,t), \text{ and } \epsilon \ell_{var}(t)\}$ where ϵ is a small quantity, and which are subject to the following conditions at the initial and final time

$$\begin{aligned} x_{var}(s, t_0) = y_{var}(s, t_0) = \theta_{var}(s, t_0) = \ell_{var}(t_0) = 0, \\ x_{var}(s, t^*) = y_{var}(s, t^*) = \theta_{var}(s, t^*) = \ell_{var}(t^*) = 0. \end{aligned} \quad (10.17)$$

The Taylor expansion of the kinematical constraint (10.3) at the first order in the small parameter ϵ implies the following relation between the variation in the rotation at the sliding sleeve exit $\theta_{var}(l - \ell(t), t)$ and the variation in the configurational parameter $\ell_{var}(t)$

$$\theta_{var}(l - \ell(t), t) = \theta'(l - \ell(t), t) \ell_{var}(t). \quad (10.18)$$

Through integration by parts, it is shown that the minimization of the functional \mathcal{A} , equation (10.16), is equivalent to the

10.2. Lagrangian and governing equations from variational approach

annihilation of following quantity

$$\begin{aligned}
& \int_{l-\ell(t)}^l \left\{ B\theta''(s, t) + N_x(s, t) \cos[\theta(s, t) + \alpha] + \right. \\
& \left. - N_y(s, t) \sin[\theta(s, t) + \alpha] \right\} \theta_{var}(s, t) ds + \\
& + \int_{l-\ell(t)}^l \{ N'_x(s, t) - \gamma \ddot{x}(s, t) \} x_{var}(s, t) ds + \\
& + \int_{l-\ell(t)}^l \{ N'_y(s, t) - \gamma (\ddot{y}(s, t) + g) \} y_{var}(s, t) ds + \\
& + \int_0^{l-\ell(t)} \{ N'_x(s, t) - \gamma \ddot{x}(s, t) \} x_{var}(s, t) ds + \\
& + \int_0^{l-\ell(t)} \{ N'_y(s, t) - \gamma (\ddot{y}(s, t) + g) \} y_{var}(s, t) ds + \quad (10.19) \\
& - \{ N_x(l, t) + m\ddot{x}(l, t) \} x_{var}(l, t) + \\
& - \{ N_y(l, t) + m(\ddot{y}(l, t) + g) \} y_{var}(l, t) + \\
& + N_x(0, t)x_{var}(0, t) + N_y(0, t)y_{var}(0, t) + \\
& + \left\{ \frac{B[\theta'(l - \ell(t), t)]^2}{2} - [N_x(l - \ell(t), t)] \sin \alpha + \right. \\
& \left. - [N_y(l - \ell(t), t)] \cos \alpha \right\} \ell_{var}(t) = 0,
\end{aligned}$$

for any variation field $x_{var}(s, t)$, $y_{var}(s, t)$, $\theta_{var}(s, t)$, and $\ell_{var}(t)$ subject to the conditions (10.17) and (10.18). It is remarked that the curvature field $\theta'(s, t)$, as well as the Lagrangian forces $N_x(s, t)$ and $N_y(s, t)$, may have a spatial discontinuity at the sliding sleeve exit $s = l - \ell(t)$. The rod's curvature within the sliding sleeve is null by definition so that the quantity $\theta'(l - \ell(t), t)$ is meant to be the rod's curvature evaluated just outside the sliding sleeve

exit, $\theta'(l - \ell(t), t) = \theta'(l - \ell^-(t), t)$. Furthermore, in equation (10.19), the symbol $[[\cdot]]$ represents the jump of the relevant function at a specific point, namely

$$[[N_j(s), t]] = \lim_{|\delta| \rightarrow 0} \left[N_j(s + |\delta|, t) - N_j(s - |\delta|, t) \right], \quad (10.20)$$

for $j = x, y$. From the minimization procedure, the equilibrium equations follow from equation (10.19) as, for the part of rod inside the sliding sleeve $s \in [0, l - \ell(t)]$

$$\begin{cases} N'_x(s, t) - \gamma \ddot{x}(s, t) = 0, \\ N'_y(s, t) - \gamma (\ddot{y}(s, t) + g) = 0, \end{cases} \quad (10.21)$$

and as

$$\begin{cases} B\theta''(s, t) + N_x(s, t) \cos[\theta(s, t) + \alpha] - N_y(s, t) \sin[\theta(s, t) + \alpha] = 0, \\ N'_x(s, t) - \gamma \ddot{x}(s, t) = 0, \\ N'_y(s, t) - \gamma (\ddot{y}(s, t) + g) = 0. \end{cases} \quad (10.22)$$

for the part of rod outside the sliding sleeve $s \in [l - \ell(t), l]$. The differential systems (10.21) and (10.22) are complemented by the boundary conditions at the rod's ends

$$\begin{cases} N_x(0, t) = N_y(0, t) = 0, \\ N_x(l, t) = -m\ddot{x}(l, t), \\ N_y(l, t) = -m(\ddot{y}(l, t) + g), \\ M(l, t) = 0, \end{cases} \quad (10.23)$$

10.3. Presence of the configurational force in dynamics

and by the interfacial boundary condition at the sliding sleeve exit, $s = l - \ell(t)$,

$$\frac{M^2(l - \ell(t), t)}{2B} = \llbracket N_x(l - \ell(t), t) \rrbracket \sin \alpha + \llbracket N_y(l - \ell(t), t) \rrbracket \cos \alpha, \quad (10.24)$$

where the constitutive relation

$$M(l - \ell(t), t) = B\theta'(l - \ell^-(t), t), \quad (10.25)$$

has been used.

10.3 Presence of the configurational force in dynamics

Considering that the internal force components N_x and N_y (along the x and y axes) can be described in terms of the components $N_{\hat{x}}$ and $N_{\hat{y}}$ (along the \hat{x} and \hat{y} axes) through the following rotation rule

$$N_x = N_{\hat{x}} \sin \alpha - N_{\hat{y}} \cos \alpha, \quad (10.26)$$

$$N_y = N_{\hat{x}} \cos \alpha + N_{\hat{y}} \sin \alpha,$$

the jump condition (10.24) at the sliding sleeve can be rewritten as

$$\llbracket N_{\hat{x}}(l - \ell(t), t) \rrbracket = \frac{M^2(l - \ell(t), t)}{2B}, \quad (10.27)$$

showing the presence of a non-null jump in the internal force component $N_{\hat{x}}$ at the sliding sleeve exit, with $N_{\hat{x}}$ representing the axial force at such a curvilinear coordinate. The presence of a jump in the axial force at the sliding sleeve is the evidence of a configurational force at this point. Therefore, such a force, which is parallel to the sliding direction and equal to

$$\frac{M^2(l - \ell^+(t), t)}{2B} \quad (10.28)$$

has always outward direction from the sliding sleeve constraint. Finally, it is worth to note that the value of configurational force within a dynamic setting coincides with that predicted under the quasi-static assumption [3].

11 The evolution of an undeformed rod suddenly released

The evolution of the system is here investigated under the assumption of negligible rod's inertia γ . Under this simplifying assumption, the mass coordinates $x(l, t) = x_l(t)$, $y(l, t) = y_l(t)$ and the configurational parameter $\ell(t)$ represent the three fundamental kinematic quantities needed to describe the entire evolution in time of the mechanical system, since the spatial integration can be independently performed in a closed form.

Indeed, when the rod's inertia is neglected, the internal actions $N_x(s, t)$ and $N_y(s, t)$ become constant in space within the two parts of the rod (inside and outside the sliding sleeve), in particular, from the integration of the differential equations (10.21)₁, (10.21)₂, (10.22)₂, (10.22)₃ considering the boundary conditions (10.23), it follows that the part of the rod within the sliding sleeve is unloaded

$$N_x(s, t) = N_y(s, t) = 0, \quad s \in [0, l - \ell(t)], \quad (11.1)$$

while the part of rod outside the sliding sleeve has constant internal force

$$\begin{aligned} N_x(s, t) &= \bar{N}_x(t), \\ N_y(s, t) &= \bar{N}_y(t), \end{aligned} \quad s \in (l - \ell(t), l], \quad (11.2)$$

where

$$\begin{aligned}\bar{N}_x(t) &= -m\ddot{x}_l(t), \\ \bar{N}_y(t) &= -m[g + \ddot{y}_l(t)].\end{aligned}\tag{11.3}$$

Therefore, the differential equation (10.22)₁ governing the rotation field $\theta(s, t)$ has coefficients varying only in time and can be rewritten as the *elastica* equation

$$B\theta''(s, t) + R(t) \sin[\theta(s, t) - \beta(t)] = 0, \quad s \in [l - \ell(t), l],\tag{11.4}$$

where $R(t)$ is the resultant force applied at the rod's end, $s = l$, and $\beta(t)$ measures its clockwise inclination with respect to the \hat{x} axis

$$\begin{aligned}R(t) &= \sqrt{\bar{N}_x^2(t) + \bar{N}_y^2(t)}, \\ \tan \beta(t) &= \frac{\bar{N}_x(t) \cos \alpha - \bar{N}_y(t) \sin \alpha}{\bar{N}_x(t) \sin \alpha + \bar{N}_y(t) \cos \alpha}.\end{aligned}\tag{11.5}$$

Note that, considering relation (10.6), the resultant force $R(t)$ and its inclination $\beta(t)$ can be also expressed in terms of the internal force components $N_{\hat{x}}$ and $N_{\hat{y}}$

$$\begin{aligned}R(t) &= \sqrt{N_{\hat{x}}^2(t) + N_{\hat{y}}^2(t)}, \\ \tan \beta(t) &= -\frac{N_{\hat{y}}(t)}{N_{\hat{x}}(t)}.\end{aligned}\tag{11.6}$$

11.1 The closed-form spatial integration

Since the governing equation (11.4) has coefficients varying only in time, the spatial integration of the *elastica* can be performed independently from that in time and in function of the unknown

11.1. The closed-form spatial integration

values $R(t)$ and $\beta(t)$ in terms of elliptic integrals. The *elastica* equation (11.4) is complemented by the boundary conditions of null rotation at the sliding sleeve exit, $\theta(l - \ell(t), t) = 0$ and of null moment at the rod's end, $\theta'(l, t) = 0$.

Following the analytical procedure seen in **Part I**, Chapter 3, the spatial integration of the differential equation (11.4) provides the relation between the resultant force $R(t)$, the end rotation $\theta_l(t)$, the resultant inclination $\beta(t)$ and the external length $\ell(t)$

$$R(t) = \frac{B}{\ell^2(t)} [\mathcal{K}(k(t)) - \mathcal{K}(m(t), k(t))]^2, \quad (11.7)$$

where $\mathcal{K}(k)$ and $\mathcal{K}(m, k)$ are, respectively, the complete and incomplete integral of the first kind,

$$\begin{aligned} \mathcal{K}(k) &= \int_0^{\pi/2} \frac{1}{\sqrt{1 - k^2 \sin^2 \phi}} d\phi, \\ \mathcal{K}(a, k) &= \int_0^a \frac{1}{\sqrt{1 - k^2 \sin^2 \phi}} d\phi, \end{aligned} \quad (11.8)$$

while $k(t)$ and $m(t)$ are parameters (varying in time) defined as functions of the end's rotation $\theta_l(t)$ and the load inclination $\beta(t)$ as follows

$$\begin{aligned} k(t) &= \sin \left(\frac{\theta_l(t) - \beta(t)}{2} \right), \\ m(t) &= -\arcsin \left[\frac{1}{k(t)} \sin \left(\frac{\beta(t)}{2} \right) \right]. \end{aligned} \quad (11.9)$$

Furthermore, the normalized position of the rod's end can be evaluated as

$$\begin{aligned}\frac{x_l(t)}{\ell(t)} &= A(t) \sin[\alpha + \beta(t)] - B(t) \cos[\alpha + \beta(t)], \\ \frac{y_l(t)}{\ell(t)} &= A(t) \cos[\alpha + \beta(t)] + B(t) \sin[\alpha + \beta(t)],\end{aligned}\tag{11.10}$$

or, equivalently,

$$\begin{aligned}\frac{\hat{x}_l(t)}{\ell(t)} &= A(t) \cos \beta(t) + B(t) \sin \beta(t), \\ \frac{\hat{y}_l(t)}{\ell(t)} &= -A(t) \sin \beta(t) + B(t) \cos \beta(t),\end{aligned}\tag{11.11}$$

where

$$\begin{aligned}A(t) &= -1 + 2 \frac{\mathcal{E}(k(t)) - \mathcal{E}(m(t), k(t))}{\mathcal{K}(k(t)) - \mathcal{K}(m(t), k(t))}, \\ B(t) &= 2k(t) \frac{\text{Cn}(\mathcal{K}(k(t)), k(t)) - \text{Cn}(\mathcal{K}(m(t), k(t)), k(t))}{\mathcal{K}(k(t)) - \mathcal{K}(m(t), k(t))},\end{aligned}\tag{11.12}$$

where $\text{Cn}(a, k)$ denotes the *Jacobi cosine amplitude* function

$$\text{Cn}(a, k) = \cos[\text{Am}(a, k)],\tag{11.13}$$

while \mathcal{E} is the incomplete elliptic integral of the second kind,

$$\mathcal{E}(a, k) = \int_0^a \sqrt{1 - k^2 \sin^2 \phi} \, d\phi.\tag{11.14}$$

It is worth remarking that the mass position, expressed through the coordinates $x_l(t)$ and $y_l(t)$, or equivalently $\hat{x}_l(t)$ and $\hat{y}_l(t)$, is fully defined by equations (11.10) and (11.11) as a function of

11.1. The closed-form spatial integration

the rod's end rotation $\theta_l(t)$, the resultant force inclination $\beta(t)$, and the external length $\ell(t)$.

12 The numerical integration in time

The dynamics of the considered elastic system can be described once the evolution in time for the three fundamental quantities $\ell(t)$, $\theta_l(t)$, and $\beta(t)$ is evaluated. The nonlinear system governing the dynamics is provided by

$$\begin{cases} \bar{N}_{\hat{x}}(t) = -m [g \cos \alpha + \ddot{\hat{x}}_l(t)] - c(t)\dot{\hat{x}}_l(t), \\ \bar{N}_{\hat{y}}(t) = -m [g \sin \alpha + \ddot{\hat{y}}_l(t)] - c(t)\dot{\hat{y}}_l(t), \\ \bar{N}_{\hat{x}}(t) = -\frac{[\bar{N}_{\hat{x}}(t)\hat{y}_l(t) - \bar{N}_{\hat{y}}(t)\hat{x}_l(t)]^2}{2B}, \end{cases} \quad (12.1)$$

which is composed by two nonlinear differential equations in time, representing the Newton's second law for the lumped mass along the \hat{x} and \hat{y} directions, plus a nonlinear equation, representing the interfacial boundary condition, equation (10.27), namely the axial equilibrium at the sliding sleeve exit in the presence of the configurational force.

More specifically, while the first two equations govern the system evolution, the third one provides an implicit relation for the values assumed by the three functions $\ell(t)$, $\theta_l(t)$, and $\beta(t)$ at the same instant t , as for example $\ell(t) = \ell(\theta_l(t), \beta(t))$.

It is remarked that the resultant component (11.3) acting on the lumped mass are modified in equations (12.1)₁ and (12.1)₂

order to take into account of dissipative effects through the non-constant parameter $c(t)$ defining the linear damping, possibly related to air drag.

Inspired by the usual definition assumed in the small amplitude dynamics of rods with fixed length,¹ the non-constant parameter $c(t)$ is considered as

$$c(t) = 2\zeta \sqrt{\frac{3mB}{\ell(t)^3}}, \quad (12.3)$$

where ζ represents a constant damping ratio.

Within a large rotation setting, all the quantities involved in the system (12.1) can be expressed as functions of the three parameters $\ell(t)$, $\theta_l(t)$, and $\beta(t)$. In particular, the spatial integration of the elastica provides the positions $\hat{x}_l(t)$ and $\hat{y}_l(t)$ through equation (11.11) while, considering equations (11.6) and (11.7), the resultant force components can be written as

$$\begin{cases} \bar{N}_{\hat{x}}(t) = -\frac{B}{\ell^2(t)} [\mathcal{K}(k(t)) - \mathcal{K}(m(t), k(t))]^2 \cos \beta(t), \\ \bar{N}_{\hat{y}}(t) = -\frac{B}{\ell^2(t)} [\mathcal{K}(k(t)) - \mathcal{K}(m(t), k(t))]^2 \sin \beta(t). \end{cases} \quad (12.4)$$

Due to the strong nonlinearities of the system (12.1) and the load components (12.4), the integration in time can be only performed numerically.

¹ In the small amplitude dynamics of a lumped mass attached at the free end of a clamped rod of length L and stiffness B , it is usually assumed

$$c = 2\zeta \sqrt{\frac{3mB}{L^3}}, \quad (12.2)$$

expression that can be retrieved from the non-constant parameter $c(t)$, equation (12.3), in the case when $\ell(t) = L$.

12.1 Initial conditions and small displacement regime

The initial condition of undeformed (rectilinear) configuration at rest is assumed for the rod so that the kinematics of the lumped mass at the initial time is given by

$$\hat{x}_l(0) = \ell_0, \quad \hat{y}_l(0) = \hat{x}_l(0) = \hat{y}_l(0) = 0, \quad (12.5)$$

where ℓ_0 is the length of the rod's outer part at the initial time, $\ell_0 = \ell(t = 0)$. Such evolutive problem, which starts from the undeformed initial configuration, is consistent with treating the dynamic problem under the assumption of negligible rod's inertia.² Moreover, because of the inextensibility assumption, a stiffening of the differential system occurs whenever the rod approaches the undeformed configuration, namely in the small displacement regime. In order to overcome this numerical issue, the integration is performed treating the small regime approximation of the nonlinear system for the time intervals when the transversal displacement satisfies the following condition

$$|\hat{y}_l(t)| < \frac{\ell(t)}{200}. \quad (12.6)$$

Within the small rotation regime, the rod's end position can be computed as

$$\begin{aligned} \hat{x}_l(t) &= \ell(t), \\ \hat{y}_l(t) &= \frac{\overline{N}_{\hat{y}}(t)\ell^3(t)}{3B}, \end{aligned} \quad (12.7)$$

²General initial conditions related to the presence of a non null curvature at the sliding sleeve exit may lead to a jump in the deformed configuration at the initial time. This would be the result of a sudden transfer of the configurational force from the sliding sleeve to the point where the external mass is located, $s = l$, and that could be more effectively modelled considering the intrinsic motion of the rod.

and the following moment inequality holds

$$\overline{N}_{\hat{x}}(t)\hat{y}_l(t) \ll \overline{N}_{\hat{y}}(t)\hat{x}_l(t), \quad (12.8)$$

so that the nonlinear system (12.1), composed by two nonlinear differential equation and one nonlinear equation, can be reduced to the following system composed by two nonlinear differential equations

$$\begin{cases} \frac{9B}{2} \frac{\hat{y}_l^2(t)}{\hat{x}_l^4(t)} = m [g \cos \alpha + \ddot{\hat{x}}_l(t)] + c\dot{\hat{x}}_l(t), \\ 3B \frac{\hat{y}_l(t)}{\hat{x}_l^3(t)} = -m [g \sin \alpha + \ddot{\hat{y}}_l(t)] - c\dot{\hat{y}}_l(t). \end{cases} \quad (12.9)$$

It is remarked that due to the small rotation assumption, the nonlinear system (12.9) is solved in terms of solely two independent quantities $\hat{x}_l(t) = \ell(t)$ and $\hat{y}_l(t)$, differently from solving the system (12.1), where $\ell(t)$ is not constrained to be equal to $\hat{x}_l(t)$. For this reason, the obtained numerical solution suffers a discontinuity in $\ell(\tilde{t})$ and $\dot{\ell}(\tilde{t})$ at all the times \tilde{t} when the numerical integration passes from treating the nonlinear system (12.1) to its approximated version (12.9) and viceversa. In particular, the integration starts considering the small rotation regime, so that the external length is constrained to be equal to the axial position, $\ell(t) = \hat{x}_l(t)$, and therefore its velocity is given by $\dot{\ell}(t) = \dot{\hat{x}}_l(t)$. When the small rotation condition (12.6) is no longer satisfied, the field $\ell(t)$ returns to be unconstrained. The value of $\ell(\tilde{t})$ and the corresponding velocity $\dot{\ell}(\tilde{t})$ at the passage time \tilde{t} can be obtained from equation (12.1)₃ and in its derivative version in time. It follows that jumps in the external length $\ell(\tilde{t})$ and its velocity $\dot{\ell}(\tilde{t})$ are originated at all the times \tilde{t} when the numerical integration passes from treating the nonlinear system (12.1) to its approximated version (12.9). Nevertheless, because the passage for the two solving systems is applied for the

12.1. Initial conditions and small displacement regime

condition (12.6), it is numerically found that the jumps in the mentioned quantities are always negligible, as shown below.

12.1.1 Dimensionless parameters and numerical integration

Introducing the characteristic time T

$$T = \sqrt{\frac{\ell_0}{g}}, \quad (12.10)$$

a parametric analysis of the system evolution in the dimensionless time variable $\tau = t/T$ can be investigated in terms of the following normalized kinematical quantities

$$\lambda(\tau) = \frac{\ell(\tau)}{\ell_0}, \quad \hat{\xi}(\tau) = \frac{\hat{x}_l(\tau)}{\ell_0}, \quad \hat{\eta}(\tau) = \frac{\hat{y}_l(\tau)}{\ell_0}, \quad (12.11)$$

at varying the sliding sleeve inclination α and the normalized load parameter p

$$p = \frac{mg\ell_0^2}{B}, \quad (12.12)$$

which condenses both the initial geometrical and loading conditions.

In the dimensionless form of the equations of motion, the non-constant parameter $c(t)$ appears through the normalized damping parameter $v(\tau) = c(\tau)T/m$, which can be rewritten in terms of the normalized load p and the normalized length $\lambda(\tau)$ as

$$v(\tau) = \frac{2\sqrt{3}\zeta}{\sqrt{p\lambda^3(\tau)}}. \quad (12.13)$$

The numerical integration considers the dimensionless version of the initial conditions (12.5),

$$\hat{\xi}(0) = 1, \quad \hat{\eta}(0) = \dot{\hat{\xi}}(0) = \dot{\hat{\eta}}(0) = 0. \quad (12.14)$$

12.1. Initial conditions and small displacement regime

and is accomplished by means of the function `NDSolve` in *Mathematica* (v. 11) considering the following options: `MaxStepSize` $\rightarrow 10^{-3}$, `StartingStepSize` $\rightarrow 10^{-8}$, `Method` \rightarrow `IndexReduction`.

The jumps inherent to the adopted numerical strategies are found to be negligible, in particular the following inequalities are observed to hold for all the passage times $\tilde{\tau}$

$$\begin{aligned} \frac{|\ell(\tilde{\tau}^+) - \ell(\tilde{\tau}^-)|}{\ell(\tilde{\tau}^-)} &< 5 \cdot 10^{-5}, \\ \frac{|\dot{\ell}(\tilde{\tau}^+) - \dot{\ell}(\tilde{\tau}^-)|}{\dot{\ell}(\tilde{\tau}^-)} &< 10^{-2}. \end{aligned} \tag{12.15}$$

Moreover, the consistency of the numerical integration is assessed comparing the increment in the total energy decrease of the system $\dot{\mathcal{V}}(\tau)$ with the power dissipated by the damper $\Pi_d(\tau) = Bv(t)p\sqrt{\dot{\xi}(\tau)^2 + \dot{\eta}(\tau)^2}/\ell_0$. With reference to the options assumed in all the analyzed evolutions, negligible discrepancies are always found between these two quantities, for which the following condition for the normalized modulus of their difference is satisfied

$$\left| \frac{\dot{\mathcal{V}}(\tau) - \Pi_d(\tau)}{\dot{\mathcal{V}}(\tau)} \right| < 2 \times 10^{-4}. \tag{12.16}$$

13 Theoretical predictions and definition of p_{cr}

With reference to a non-null (initial) length ℓ_0 , the equilibrium configuration has been disclosed from quasi-static analysis for a specific pair of values p and α satisfying [3]

$$p_{eq} = \left[\mathcal{K} \left(\frac{1}{2} \right) + \mathcal{K} \left(\arcsin \left(\frac{1}{\sqrt{2}} \sin \frac{\alpha}{2} \right), \frac{1}{2} \right) \right]^2, \quad (13.1)$$

representing the geometrical condition of orthogonality between the rod's end tangent and the applied load direction, and which can be approximated for inclinations $\alpha \simeq 0$ and $\alpha \simeq \pi/2$ as

$$\begin{aligned} p_{eq}(\alpha) &\approx \mathcal{K} \left(\frac{1}{2} \right) \left[\mathcal{K} \left(\frac{1}{2} \right) - \sqrt{2}\alpha \right]^2 + o(\alpha), \\ p_{eq}(\alpha) &\approx \pi - 2\alpha + o(\pi - 2\alpha)^2. \end{aligned} \quad (13.2)$$

Being this configuration unstable, it is expected that the dynamic effects originated from any perturbation applied to the system will push towards the minimization or the maximization of the external length $\lambda(\tau)$ at infinite time. Therefore, two final configurations may be approached by the system, the complete injection/ejection into/from the sliding sleeve constraint, respectively corresponding to the lower and upper bounds of the physically relevant set for the configurational parameter, $\lambda(\tau) \in [0, \bar{\lambda}]$ where $\bar{\lambda} = l/\ell_0$.

Although from the theoretical point of view, the transition between these two opposite behaviours would occur for a dimensionless load $p_{tr}(\alpha)$, its analytical definition becomes in general impossible within a dynamic framework governed by strongly nonlinear equations.

From the practical point of view, considering as initial state the sudden release of the system from the undeformed state, the limit value $\lambda(\tau \rightarrow \infty)$ attained by the system for a specific pair of values p and α can be disclosed introducing dissipative effects¹ within the equations of motion, equations (12.1) and (12.9).

In particular, two sets of value p are recognized as corresponding to the final stages of complete injection and complete ejection through numerical simulations as follows

$$\begin{aligned} p \in (0, p_{tr}(\alpha)) &\rightarrow \text{injection}, \\ p \in (p_{tr}(\alpha), \infty) &\rightarrow \text{ejection}. \end{aligned} \tag{13.3}$$

The transition value $p = p_{tr}(\alpha)$ is numerically evaluated for a specific inclination angle α through the following iterative method at increasing step number j . At the j -th step, the transition value $p = p_{tr}^{(j)}(\alpha)$ is estimated as

$$p_{tr}^{(j)}(\alpha) = \frac{p_{max,in}^{(j)}(\alpha) + p_{min,out}^{(j)}(\alpha)}{2} \tag{13.4}$$

where $p_{max,in}^{(j)}(\alpha)$ and $p_{min,out}^{(j)}(\alpha)$ are respectively the highest load for the rod injection and the lowest load for ejection known at the step j . The iterative procedure is stopped at the step k and

¹In absence of dissipation, the system always reaches the final stage of complete ejection, because the finite energy of the system can not be converted into kinetic energy only along the axial direction. This issue will be analyzed more specifically in a future work.

the transition value is considered reached, $p_{tr} = p_{tr}^{(k)}$ when the difference in the estimation with the previous step is negligible. In the present analysis, this is considered to be given by

$$\left| \frac{p_{tr}^{(k)} - p_{tr}^{(k-1)}}{p_{tr}^{(k-1)}} \right| < 5 \times 10^{-4}. \quad (13.5)$$

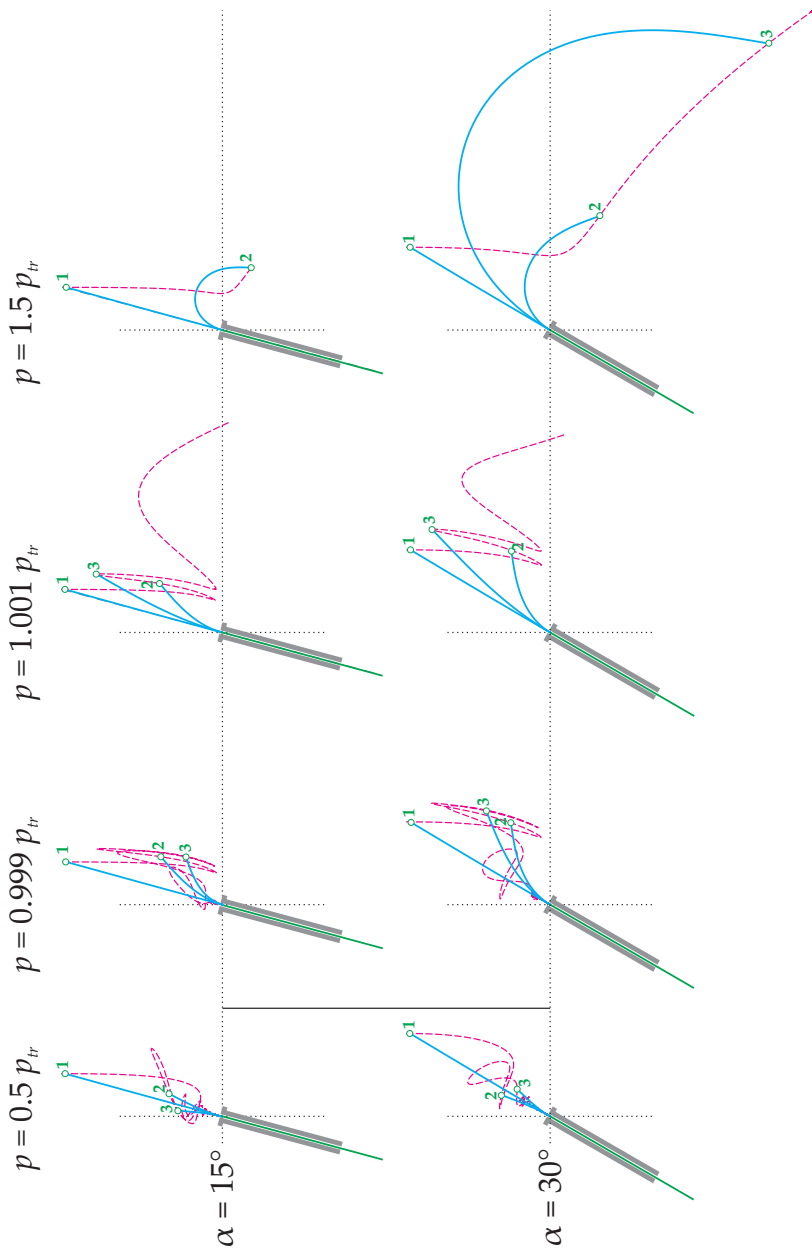


FIG. 13.1: Trajectories of the suddenly released mass within the dimensionless plane $x/\ell_0 - y/\ell_0$ for $\alpha = 15^\circ$ (first line), $\alpha = 30^\circ$ (second line) different values of the dimensionless load $p = \{0.5, 0.999, 1.001, 1.5\} p_{cr}(\alpha)$ where the load values are increased from the left to the right. The critical dimensionless loads are numerically computed to be approximately $p_{tr}(\alpha = 15^\circ) \simeq 9.87$, $p_{tr}(\alpha = 30^\circ) \simeq 3.74$. Deformed configurations are reported, attained at the dimensionless times $\tau_1 = 0.2$, $\tau_2 = 2$ and $\tau_3 = 3$.

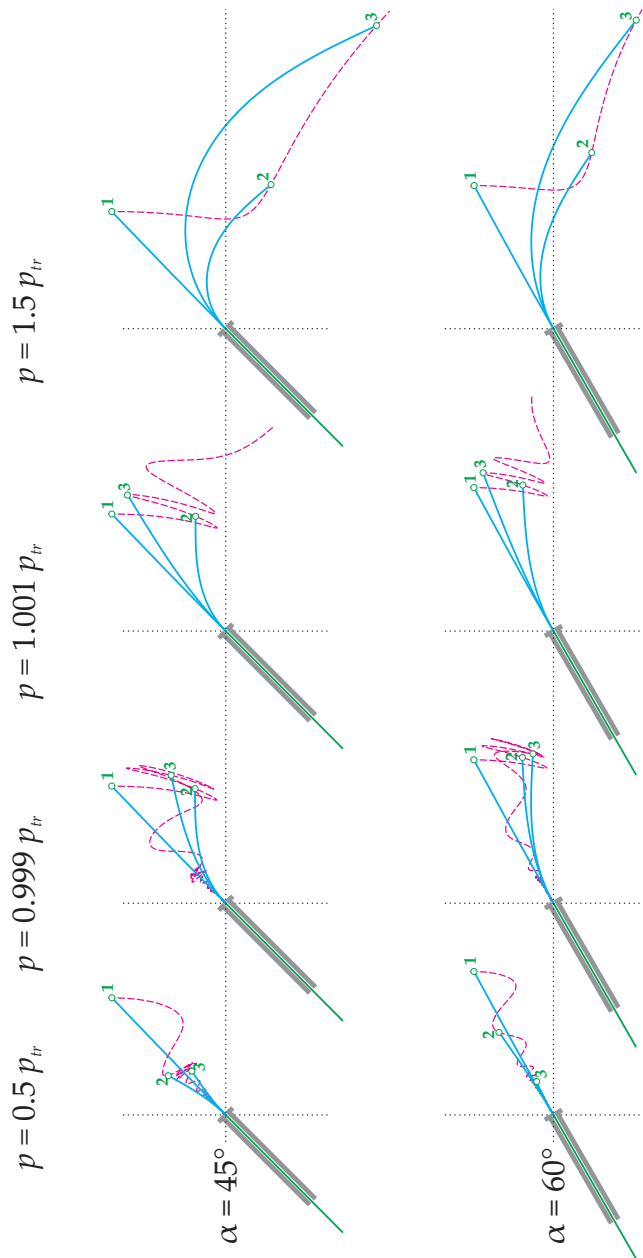


FIG. 13.2: Trajectories of the suddenly released mass within the dimensionless plane $x/\ell_0 - y/\ell_0$ for $\alpha = 45^\circ$ (first line) and $\alpha = 60^\circ$ (second line) at different values of the dimensionless load $p = \{0.5, 0.999, 1.001, 1.5\} p_{tr}(\alpha)$ where the load values are increased from the left to the right. The critical dimensionless loads are numerically computed to be approximately $p_{tr}(\alpha = 45^\circ) \simeq 1.84$ and $p_{tr}(\alpha = 60^\circ) \simeq 0.946$. Deformed configurations are reported, attained at the dimensionless times $\tau_1 = 0.2$, $\tau_2 = 2$ and $\tau_3 = 3$.

The two regions corresponding to the rod's injection or ejection are reported in Fig. 13.3, where the separating curve represented the critical value $p_{tr}(\alpha)$.

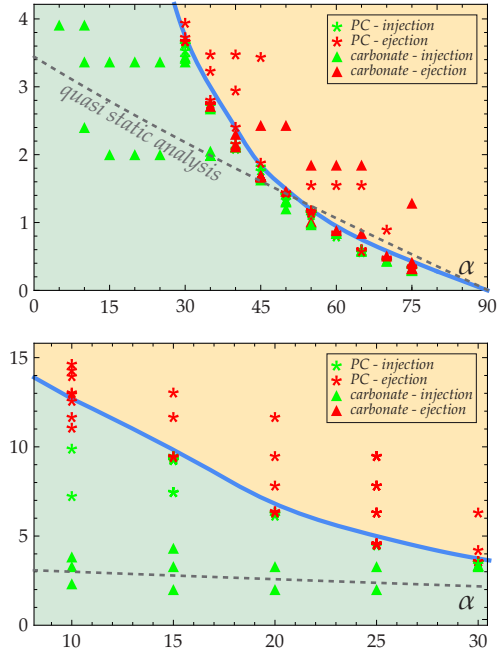


FIG. 13.3: Map of the regions identifying the pairs of dimensionless load p and sliding sleeve inclination α for which injection ($p < p_{tr}$, green region) and ejection ($p \geq p_{tr}$, yellow region) occur when an undeformed rod at rest is suddenly released. The transition between these two behaviours is defined by the curve $p_{tr}(\alpha)$. Experimental results are also reported (see Chapter 14).

To provide further insights about the system evolution, the normalized external length $\lambda(\tau) = \ell(t)/\ell_0$ and its phase portrait is reported at varying the normalized load p and sliding sleeve inclination α in Fig. 13.4.

It can be observed that:

- when $p < p_{tr}$, the oscillations can be described as the repetition of two stages. A decreasing amplitude stage is followed by an increasing amplitude stage up to a return to 'approximately' the initial condition (from below). As time increases, since dissipation is considered, the oscillations are reduced and the final injection of the rod is attained.
- when $p > p_{tr}$, when oscillations occur, these have increasing amplitude in time towards the eventual complete ejection of the rod from the sliding sleeve. At an initial stage of the oscillations, the time derivative of the external length changes repetitively sign. Oscillations may be absent during the entire system evolution when a very large load p is imposed.

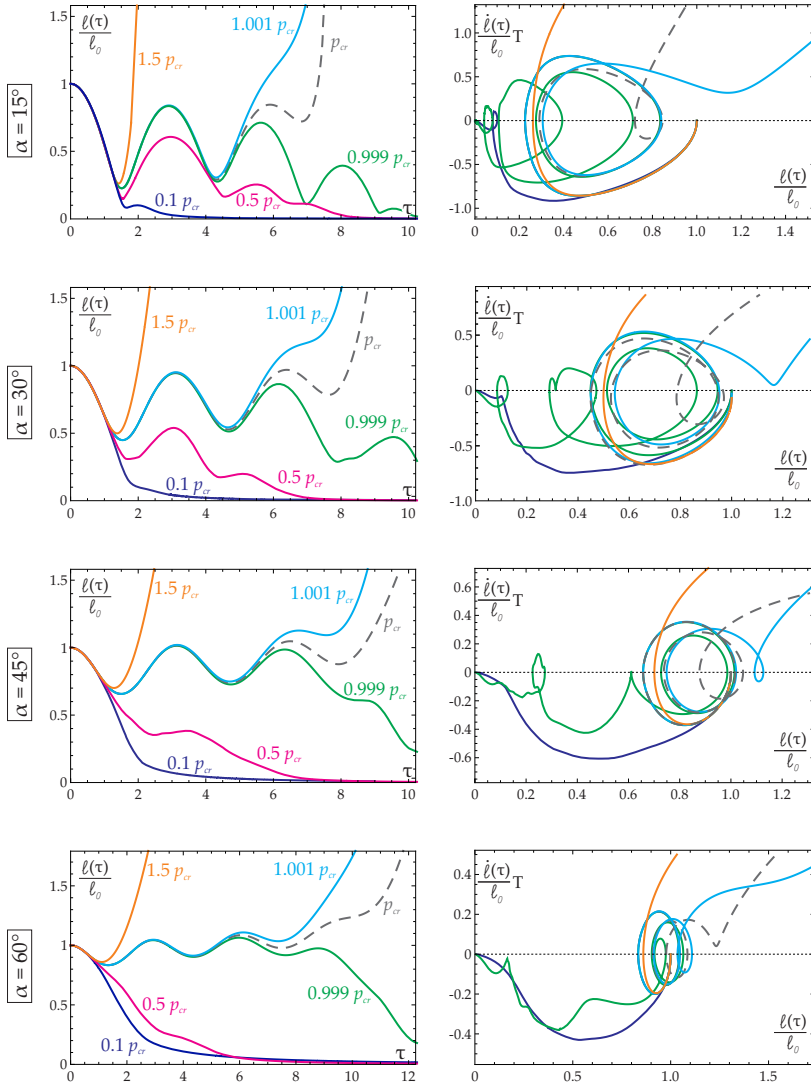


FIG. 13.4: (Left part) Evolution in the dimensionless time τ is reported for of the external length $\ell(\tau)$ at different values of the sliding sleeve inclination, $\alpha = \{15^\circ, 30^\circ, 45^\circ, 60^\circ\}$ and values of the dimensionless load $p = \{0.1, 0.5, 0.999, 1, 1.001, 1.5\} p_{tr}(\alpha)$. (Right part) For the same values of α , phase portrait of $\ell(\tau)$, namely how the velocity $\dot{\ell}(\tau)$ varies with $\ell(\tau)$, is reported for $p = \{0.1, 0.999, 1, 1.001, 1.5\} p_{tr}(\alpha)$.

14 Experimental analysis

An experimental set up (Fig. 14.1) was designed and realised to validate the theoretical predictions.

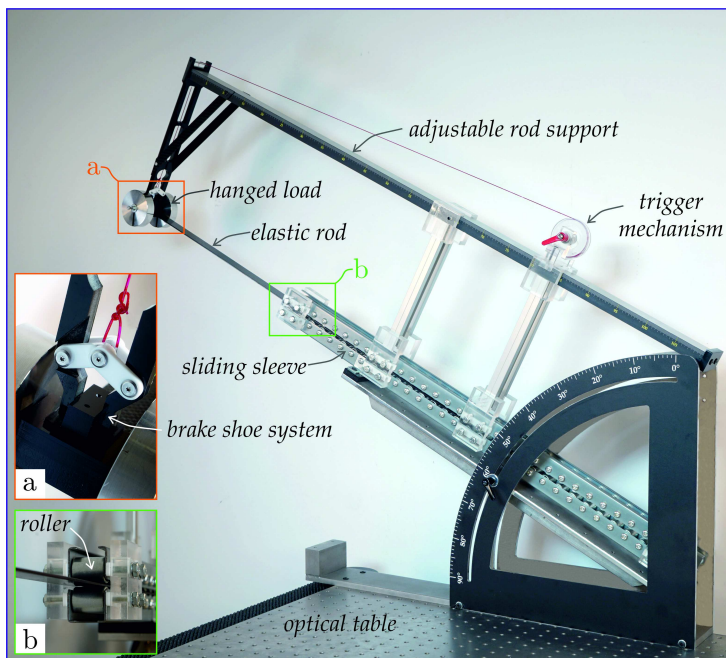


FIG. 14.1: The experimental set-up realised to investigate the dynamical behaviour of the considered structural system. Insets (a) and (b) report the details of the release mechanism and the sliding sleeve realization, respectively.

The sliding sleeve, which has an overall length of 825 mm, is realised with 33 pairs of rollers (Fig. 14.1b). Each roller is made up of a Steel cylinder of 20 mm diameter and 25 mm length, containing two rollers bearings. In the previous work restricted to the quasi-static case [3], it is proven that such a roller device is capable of providing a configurational force predicted by the theoretical model. In order to obtain the initial rectilinear (undeformed) condition, the rod is attached to a brake shoe system (Fig. 14.1a) which is placed on a rigid support. The rigid support allows also to set the initial length of the beam outside the sliding sleeve, ℓ_0 . Through a fishing wire, the brake shoe system is connected to a thightner and a trigger, so that it can be easily controlled to obtain the sudden release of the rod. The whole apparatus is mounted on a pneumatic optical table (Nexus from ThorLabs), in order to prevent any spurious vibration.

Tests were performed using three different elastic rods, two made up from polycarbonate (PC) strips (Young Modulus $E = 2350$ MPa and volumetric mass density $\rho = 1180$ kg/m³), while one rod was made up from carbon fibre strips ($E = 80148$, $\rho = 1620$ kg/m³). The PC rods are both 2.95 ± 0.05 mm thick and 25 ± 0.05 mm wide, but differ in their length (550 mm and 800 mm). The carbon rod is 2.0 ± 0.05 mm thick, 25 mm wide and 800 mm long. All the rods were shaped by cutting plain sheets with an engraving machine (Roland EGX-600). A tolerance of 0.5 mm was kept between the rods and the rollers along the channel. Moreover, at the beginning of each test, the rods were sprayed with a lubricant oil (Ballistol by Klever) in order to minimize the friction between the sliding sleeve. High frame-rate movies (240 fps) are recorded during each test with a Sony PXW-FS5 video camera, to fully capture the dynamic motion of the rods. All photos are taken with a Sony Alpha 9 camera.

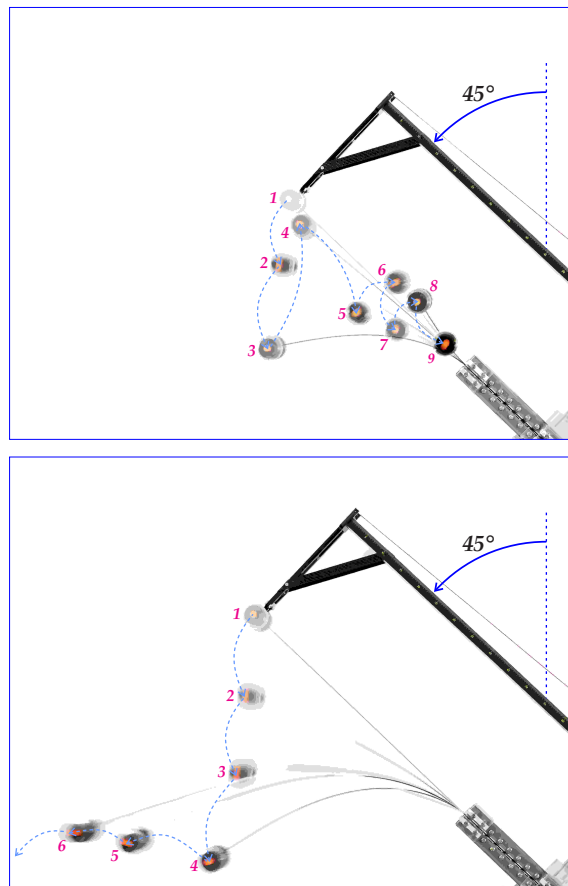


FIG. 14.2: Results of the test obtained for $p = 0.75p_{cr}$ (upper part) and $p = 1.1p_{cr}$ (lower part) for $\alpha = 45^\circ$. The experimental test confirm the transition between the two possible behaviours theoretically predicted.

Several tests were performed at varying both the inclination angle α and the dimensionless load p , obtained varying the lumped mass m and the initial lengths ℓ_0 . In Fig. (13.3) all the performed tests are reported, identifying the pairs of dimensionless load p and sliding sleeve inclination α . Moreover, in Fig. (14.2) the results of two test performed for $\alpha = 45^\circ$ are reported, showing the transition between the two possible behaviours, for which the rod approaches the final stage of complete injection (when $p = 0.75p_{cr}$, upper part) or the final stage of complete ejection (when $p = 1.1p_{cr}$, lower part).

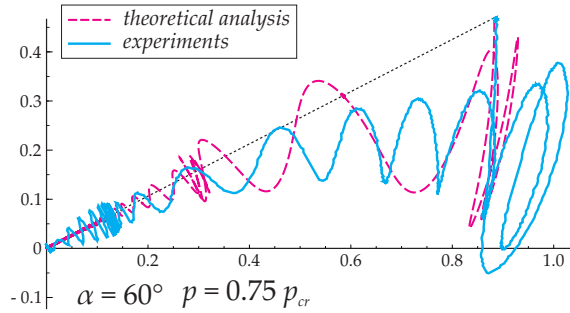


FIG. 14.3: Comparison between the trajectory travelled by the lumped mass during an experimental test performed with the carbon rod and that predicted by the theoretical analysis, obtained for $\alpha = 60^\circ$ and for a dimensionless load $p = 0.75p_{cr}$.

Finally, an *ad hoc* application was developed in Python in order to process the videos acquired at high frame-rates. The code exploits the OpenCV libraries, a tool-set dedicated to image processing and machine learning applications. The developed program tracks the trajectory travelled by the lumped mass, providing its position x_l, y_l as output at each frame. Fig. 14.3 shows an example of the comparison between the trajectory

travelled by the lumped mass during an experimental test performed with the carbon rod and that predicted by the theoretical analysis, obtained for $\alpha = 60^\circ$ and for a dimensionless load $p = 0.75p_{cr}$.

All the experiments were performed at the Instabilities Lab of the University of Trento.

15 Conclusion

The presence of configurational forces acting on elastic structures has been theoretically proven within a dynamic framework, extending a previous proof restricted to the quasi-static case [3]. The sudden release from the undeformed configuration has been analyzed for a rod constrained by a frictionless sliding sleeve and with a lumped mass applied to the other end. A simplified model based on the spatial integration of the elastica has been exploited to disclose the behaviour of the nonlinear dynamical response, defining the evolution of the configurational parameter corresponding to the length of the rod outside the constraint. Through a variational approach, the presence of a configurational force within the dynamical setting has been proven to coincide with that predicted within the quasi-static setting. It has been shown that the configurational force, generated at the exit of the sliding sleeve, dramatically affects the mechanical response of the system, defining two different types of evolution for the system, for which the rod approaches the final stage of complete injection or the final stage of complete ejection. The theoretical predictions have been validated with a specifically designed experimental set-up.

The obtained results open new perspectives in the analysis of the dynamic response of structural systems subject to configurational constraints and pave the way to the mechanical design of innovative flexible devices for advanced applications.

The results presented in the second part of the thesis are going to be soon submitted for publication in a peer-reviewed International journal.

Bibliography

- [1] Batista, M. (2016). Comment on 'Longest reach of a cantilever with a tip load'. *European Journal of Physics*, 37 (5), 058004.
- [2] Bigoni, D. (2012) *Nonlinear solid mechanics: bifurcation theory and material instability*. Cambridge University press.
- [3] Bigoni, D., Dal Corso, F., Bosi, F. and Misseroni, D. (2015) Eshelby-like forces acting on elastic structures: theoretical and experimental proof. *Mech. Mater.*, 80, 368–374.
- [4] Bigoni, D., Dal Corso, F., Misseroni, D. and Bosi, F. (2014) Torsional locomotion *Proc. Roy. Soc. A*, 470.2171, 20140599.
- [5] Bishopp KE, Drucker DC. (1945) *Large deflection of cantilever beams*. Armour Research Foundation.
- [6] Bosi, F., Misseroni, D., Dal Corso, F. and Bigoni, D. (2014) An elastica arm scale. *Proc. Roy. Soc. A*, 470, 20140232
- [7] Bosi, F., Misseroni, D., Dal Corso, F. and Bigoni, D. (2015). Development of configurational forces during the injection of an elastic rod. *Extreme Mechanics Letters*, 471, 83–88.
- [8] Broman, A. (1970). *Introduction to partial differential equations: from Fourier series to boundary-value problems*. Addison-Wesley series in applied Mathematics. London: Addison-Wesley.
- [9] Cicconofri, G., DeSimone, A. (2015) A study of snake-like locomotion through the analysis of a flexible robot model. *Proc. R. Soc. A* 471, 2184.

- [10] Clauvelin, N., Audoly, B., Neukirch, S. (2009) Matched asymptotic expansions for twisted elastic knots: a self-contact problem with non-trivial contact topology. *J. Mech. Phys. Solids*, 57 (9), 1623–1656.
- [11] da Vinci, Leonardo, *Il Codice Atlantico della Biblioteca ambrosiana di Milano*. Giunti Editore.
- [12] Eshelby, J.D. (1951) The force on an elastic singularity. *Phil. Trans. Roy. Soc. London A*, 244-877, 87–112.
- [13] Eshelby, J.D. (1956) The continuum theory of lattice defects. *Solid State Phys.*, 3.C, 79–144.
- [14] Eshelby, J.D. (1970) Energy relations and the energy-momentum tensor in continuum mechanics. in *Inelastic Behaviour of Solids* (eds. M. Kanninien, W. Adler, A. Rosenfield and R. Jaffee), 17–115, McGraw-Hill, New York.
- [15] Eshelby, J.D. (1975) The elastic energy-momentum tensor. *Journal of Elasticity*, 5.3-4, 321–335.
- [16] Essebier, S, Baker, G. (1995) Computational techniques for nonlinear dynamics of continuous systems. *J. Eng. Mech.* 121, 1193–1199.
- [17] Fotouhi R. (2007) Dynamic analysis of very flexible beams. *Journal of Sound and Vibration* 305, 521–533.
- [18] Frere, J., L’Hermette, M., Slawinski, J., Tourny-Chollet, C. (2010) Mechanics of pole vaulting: a review. *Sports Biomechanics* 9 (2), 123–138.
- [19] Gans R. F. (1992) On the dynamics of a conservative elastic pendulum. *ASME Journal of Applied Mechanics* 59, 425–430.
- [20] Hsiao, K.-M., Jang, J.-Y. (1991) Dynamic analysis of planar flexible mechanisms by co-rotational formulation, *Computer Methods in Applied Mechanics and Engineering* 87, 1–14.
- [21] Hubbard, M. (1980) Dynamics of the pole vault, *Journal of Biomechanics* 13 (11), 695–976.
- [22] Kovac, M. (2016) Learning from nature how to land aerial robots. *Science*, 352, 895–896.

BIBLIOGRAPHY

- [23] Laschi, C., Cianchetti, M., Mazzolai, B., Margheri, L., Follador, M., Dario, P. (2012) Soft robot arm inspired by the octopus. *Adv. Robotics* 26, 709–727
- [24] Levyakov, S.V., Kuznetsov, V.M., (2010) Stability analysis of planar equilibrium configurations of elastic rods subjected to end loads *Acta Mech.* 211.1-2, 73–87.
- [25] Love, A.E.H. (1927) *A treatise on the mathematical theory of elasticity*. Cambridge University Press.
- [26] Mahvash, M. Dupont, P.E. (2011) Stiffness Control of Surgical Continuum Manipulators *IEEE Tran. on Robotics* 27 (2), 334–345
- [27] Majidi, C. (2013) Soft Robotics – A Perspective: Current Trends and Prospects for the Future. *Soft Robotics* 1, 5–11.
- [28] Meek, J.L., Liu, H. (1995) Nonlinear dynamics analysis of flexible beams under large overall motions and the flexible manipulator simulation, *J. Comp. Struct.* 56, 1–14.
- [29] Polygerinos, P., Wang, Z., Galloway, K.C., Wood, R.J., Walsh, C.J. (2015) Soft robotic glove for combined assistance and at-home rehabilitation. *Robotics and Autonomous Systems* 73, 135–143.
- [30] Puglisi, G., Truskinovsky, L. (2002) Rate independent hysteresis in a bi-stable chain. *J. Mech. Phys. Solids*, 50 (2), 165–187.
- [31] Puglisi, G., Truskinovsky, L. (2005) Thermodynamics of rate-independent plasticity. *J. Mech. Phys. Solids*, 53 (3), 655–679.
- [32] Rus, D., Tolley, M.T. (2015) Design, fabrication and control of soft robots. *Nature* 521, 467–475.
- [33] Simo, J.C., Vu-Quoc, L. (1986) On the dynamics of flexible beams under large overall motions-the plane case: part ii, *ASME Journal of Applied Mechanics* 53, 855–863.

- [34] Snyder, J.M., Wilson, J.F. (1990) Dynamics of the elastica with end mass and follower loading. *J. Appl. Mech.* 57, 203–208.
- [35] Trivedi, D., Rahn, C.D., Kier W.M., Walker, I.D. (2008) Soft robotics: Biological inspiration, state of the art, and future research. *Appl. Bionics Biomech.* 5, 99–117.
- [36] Xiao, J., and Chen, X. (2013) Buckling morphology of an elastic beam between two parallel lateral constraints: implication for a snake crawling between walls. *J. R. Soc. Interface* 10, 20130399.
- [37] Yang, D., Mosadegh, B., Ainla, A., Lee, B., Khashai, F., Suo, Z., Bertoldi, K., Whitesides, G.M. (2015) Buckling of Elastomeric Beams Enables Actuation of Soft Machines. *Adv. Mater.* 27, 6323–6327.
- [38] Wang, C.Y. (1981). Large deflections of an inclined cantilever with an end load. *Int. J. Non-linear Mech.*, 16 (2), 155–164.
- [39] Wang, C.Y. (2016). Longest reach of a cantilever with a tip load. *European Journal of Physics*, 37 (1), 012001.
- [40] Wilson, J.F., Li, D., Chen, Z., George, R.T. (1993) Flexible robot manipulators and grippers: relatives of elephant trunks and squid tentacles. In: *Robots and biological systems: toward a new bionics?* NJ, USA: Springer-Verlag New York, Inc., p. 474–479.
- [41] Zhou, X., Majidi, C., O'Reilly, O.M. (2015) Soft hands: An analysis of some gripping mechanisms in soft robot design. *Int. J. Solids and Structures* 64–65, 155–165.